Unlocking the Eastern Mediterranean Sea salinity history for the last 350.000 years

Lynn Kruithof

Supervisors: Prof. dr. Gert-Jan Reichart, Esmee Geerken, dr. Rick Hennekam

Table of Contents

Abstract

The Eastern Mediterranean Sea is impacted by North African monsoon variability and high-latitudinal climate processes leading to large-scale surface water density (temperature/salinity) variability and related overturning circulation changes on orbital timescales. Intensification of monsoon rainfall in northern Africa, induced by precessional changes, is seen as the main driver of increased freshwater input from the Nile River during periods where distinct organic-rich layers (i.e., sapropels) were deposited in the Eastern Mediterranean Sea. These sapropel intervals are thought to be the result of enhanced Nile River (and potential other North African rivers) run-off influencing O_2 transport to the deep sea by density stratification, with concurrent increase in organic matter production. As especially salinity is an important parameter to cause this density stratification, it is of pivotal importance to have proxies that accurately predict past salinity in order to fully get a grip to the conditions that can lead to anoxia during sapropels. This thesis therefore thoroughly tests a range of salinity proxies ($\delta^{18}O$, Ba/Ca, Na/Ca, and Mg/Ca) of the planktic foraminifer *G. ruber* from the Eastern Mediterranean Sea to shed light on the African monsoon variability and its impact on Eastern Mediterranean circulation over the last 350.000 years. We find that the $\delta^{18}O$ record shows variability that is mainly dominated by Nile River run-off whereas the Element to Ca ratios show more complex patterns. Our Mg/Ca record shows a strong precession-related signal with lower values during sapropels and higher values outside of these events. This suggests that salinity has an strong effect on foraminiferal Mg/Ca, especially for non-sapropel times, but the exact processes involved remain elusive. Higher Na/Ca ratios in sapropels indicates a better preservation of the Na signal under anoxic conditions, preventing loss of Na due to oxidation and leaching. Whereas, in non-sapropel periods the Na appears to diffuse from the calcite lattice. The Ba/Ca is more in tune with the $\delta^{18}O$ record, with higher values during intervals of high Nile discharge as a consequence of the inflow of Ba-enriched river water. The run-off based Ba/Ca and $\delta^{18}O$ record show that the timing and pace of the North African monsoon during the Holocene to late Pleistocene was near-synchronous with the West African monsoon. The onset of enhanced West African monsoon precipitation lags behind the North African monsoon during glacial-interglacial transitions. The early peak of monsoon fuelled intensification of rainfall in North Africa, being synchronous with variability observed in Asian monsoon records, suggests a major influence of an Indian Ocean moisture source on North African monsoon during this transition, whereas today the Atlantic Ocean is the dominant water source fuelling the North African monsoon. The delayed response of the West African monsoon appears to be related to persistent meltwater pulses into the North Atlantic Ocean, slowing down the Atlantic Meridional Overturning Circulation and delaying monsoon intensification in that area. The $\delta^{18}O$ record also shows that deep-water anoxia was primarily sensitive to monsoon forcing with a secondary importance of sea-level height depending on their magnitudes. Monsoon forcing seemed to be more important for sapropels S3, S4, S5, S6, S7 and S8, whereas a strong impact of sea-level cannot be excluded for sapropels S1, S9 and S10. The euxinia (i.e., depletion of oxygen with raised levels of free hydrogen sulphide) proxy Mo shows that the deep-water anoxia development was more progressive for sapropels S7, S9 and S10, and more rapid for sapropels S3, S4, S5, S6 and S8. This suggests, at least, a threshold response to forcing for sapropels S3, S4, S5, S6 and S8.

1   Introduction

The Eastern Mediterranean Sea (EMS) forms an extraordinary rich archive of past oceanographic and climatic changes due to its sensitivity to the North African monsoon and higher-latitude climate processes (Woodward, 2009; Rohling et al., 2015). The intensity of the African summer monsoon, associated with the Inter Tropical Convergences Zone (ITCZ), is mainly controlled by the amount of solar radiation at low latitudes, modulated by the Earth's astronomical precessional cycle (Rossignol-Strick, 1985; Rohling, 1994). The moisture that fuels the monsoonal system originates mainly from the tropical Atlantic Ocean and the southern Indian Ocean. Although the system does not penetrate into the Mediterranean itself, the monsoonal precipitation influences the hydrology of the Eastern Mediterranean indirectly through changes in Nile River discharge. Hence, the Nile catchment works as a gauge for northeast African monsoon precipitation, and reconstructions of Nile discharge hence hold climatic information about the whole northeast African continent.

Today, the main source of freshwater into the Eastern Mediterranean Sea is the Nile River. The rate of Nile River discharge is strongly affected by orbitally controlled changes in the intensity and northward penetration of the North African monsoon precipitation (e.g. Rossignol-Strick et al., 1982; Rohling et al., 2002, 2004; Osborne et al., 2008). Most of the annual Nile River discharge (70%) derives from the Blue Nile and Atbara Rivers, which originate from the Ethiopian Highlands in sub-tropical east Africa; and the remaining 30% derives from the White Nile, which originates from the Equatorial African mountain ranges (Adamson et al., 1980; Williams et al., 2000). The two main moisture sources of the Nile catchment are the Atlantic Ocean (Blue Nile) and the Atlantic/Indian system (White Nile), and the influence of each moisture source varied in the past (Hennekam et al., 2014; Costa et al., 2014). Ultimately, variability in the northeast African monsoon causes changes in the Eastern Mediterranean Sea surface salinity. Vice versa, reconstructions of eastern Mediterranean Sea surface salinity (SSS) can thus be used to reconstruct northeast African monsoon intensity. In this MSc thesis, the SSS is reconstructed using geochemical proxies to explore past variability in the northeast African monsoon. In addition, climate reconstructions will provide the background against which two major northern African migration events of modern humans will be evaluated.

Marine sediment records from the Eastern Mediterranean Sea are excellent archives that can be used to reconstruct changes in sea surface salinity based on the chemistry of planktic foraminiferal shells. Quaternary marine sediment records in this area are characterized by rhythmic deposition of organic-rich layers (sapropels), which are closely associated with periods of increased Nile River discharge into the Eastern Mediterranean Sea. Strengthening and northward migration of North African monsoon precipitation during boreal summer insolation maxima are generally viewed as a key source for these periods of increased Nile River discharge during sapropel formation (e.g. Rossignol-Strick,1985; Rohling et al., 2004; Osborne et al., 2008). The enhanced run-off of Nile River water may have either increased primary productivity and/or increased preservation of organic matter in the sediments because of inhibited water mass circulation, which leads to deep water anoxia due to O_2 consumption during ongoing organic matter degradation (e.g. Rohling et al., 2015). The collapse of the circulation during sapropels occurred rather abruptly (~50 years during sapropel S5; Marino et al., 2007) in comparison to the more gradual change in Nile discharge. This implies that the deep-sea O_2 response to forcing has clear tipping points, but to date it is unknown whether this response stays consistent under varying environmental/climatic conditions. Therefore, in this thesis the deep-sea anoxic intensity is reconstructed using redox-sensitive trace elements (i.e., Mo) (Tribovillard et al., 2006), and compared to our SSS proxies (that are associated to the primary monsoon forcing of sapropels) to see if the system response varies depended on the environmental conditions.

This study will focus on a marine sediment core 64PE406-E1 from the eastern Mediterranean to reconstruct past variability of Eastern Mediterranean Sea surface salinity during the last 350,000 years BP (Figure 1). This core is directly influenced by the outflow of the Nile River, and thus ideal to monitor past variations in salinity. Therefore, we here study the elemental composition (Ba/Ca, Na/Ca, Mg/Ca and Sr/Ca) and oxygen isotope ratios (δ^{18}O) in shells of surface-dwelling planktic foraminifera *Globigerinoides ruber* (white), which dwells at the upper 50m of the water column (Gonzalez-mora et al., 2008; Grazzini et al., 1990; Pujol and Grazini, 1995). We use Ba/Ca and δ^{18}O to reconstruct the temporal variability in Nile River run-off into the EMS. Mg/Ca in foraminiferal calcite is mainly controlled by temperature (Lea et al., 1999; Dekens et al., 2002; Anand et al., 2003; Ferguson et al., 2008) and can be used to correct foraminiferal δ^{18}O for the sea surface temperature (SST) effect, in order to obtain the salinity-related δ^{18}O (Rohling and Bigg, 1998). However, previous studies showed that, salinity (Ferguson et al., 2008; Kisakürek et al., 2008) and overgrowths of non-biogenetic calcite could affect the foraminiferal Mg/Ca ratio (Hoogakker et al., 2009; Kontakiotis et al., 2011; 2017). This adds uncertainty to the use of Mg/Ca in determining past sea surface salinity (SSS) estimates uncertain. Additionally, the oxygen isotope record is compared to a Na/Ca based salinity record, to test the applicability of this new proxy down core and better quantify the past salinity variability that occurred through Nile River outflow variability. The salinity proxy data is complementary to available sediment trace metal data (Mo) obtained from XRF core scanning, that can be used to reconstruct bottom-water anoxia strength during sapropels (e.g. Tribovillard et al., 2006).

Ultimately, these results are used to address the following questions: (1) What is the main forcing mechanism of Northeast African monsoon variability and are there any other important factors apart from insolation? (2) Are phases of increased intensity of the Northeast African monsoon linked to human dispersal out of Africa? (3) How does the strength in monsoon variability relate to the observed anoxia strength variability during sapropel formation? (4) What is the anoxia response of the Mediterranean Sea during sapropels (e.g. linear, threshold, and/or hysteresis response to forcing?
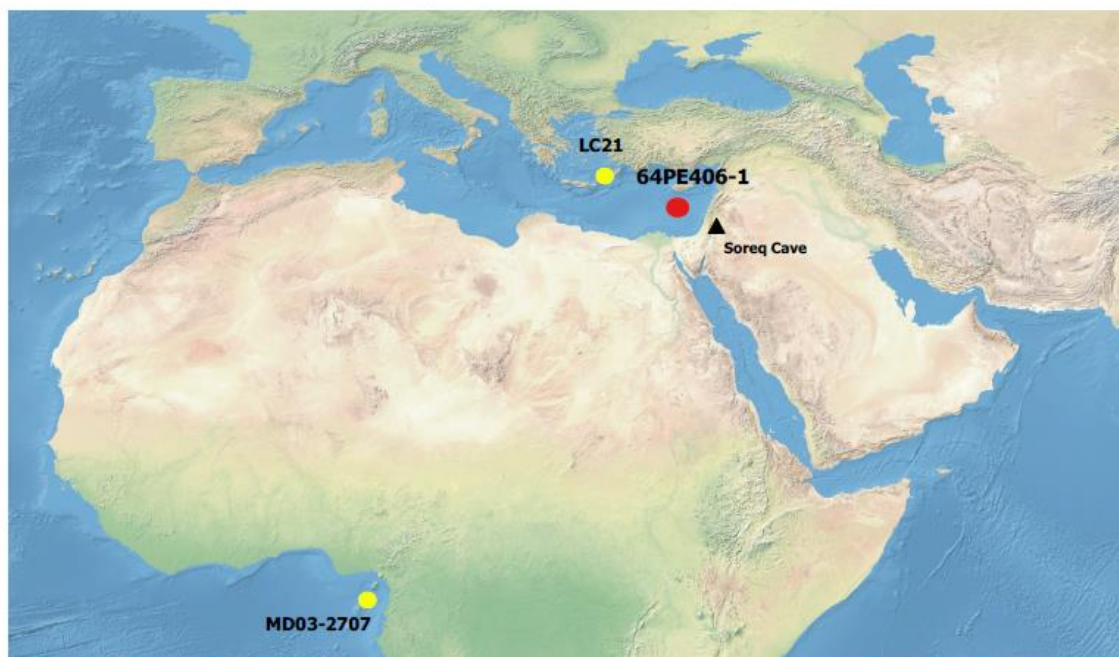

Figure 1 | Map of the eastern Mediterranean Sea (EMS) showing the core location 64PE406-E1 used in this study and cores LC21 and MD03-2707 discussed in this study**.**

2 Oceanographic setting

The Mediterranean Sea is a semi-enclosed basin that is only connected to the Atlantic Ocean through the narrow Strait of Gibraltar. Present-day Mediterranean Sea circulation is characterized by an anti-estuarine circulation pattern (Tomczak and Godfrey, 1994). Low-salinity Atlantic surface water enters through the Strait of Gibraltar where it mixes with upwelled cooler and saltier Mediterranean intermediate and deep waters (Rohling et al., 2015; Rogerson et al., 2012). The salinity increases as it flows eastward through excess evaporation, forming Modified Atlantic Water (MAW). This MAW flows anticlockwise along the African coast off the Nile River (Pinardi and Masetti, 2000). Between Cyprus and Rhodes, the saline MAW is cooled down by cold winter winds and forms Levantine Intermediate Water (LIW). The newly formed water occupies the depth of 200-500 m in the Levantine Sea and spread over the Mediterranean basin as it flows westward through the Siculo-Tunisian Strait (Wüst, 1961; Tomczak and Godfrey, 1994). Eastern Mediterranean Deep Water (EMDW) is an admixture consisting of LIW and Adriatic surface water cooled during winter. EMDW occupies the depth below 600 m and is less saline but colder and denser than LIW (Tomczak and Godfrey, 1994). Before damming of the Nile River, a distinct freshwater anomaly occurred in the southeast of the Levantine Basin (Hecht and Gertman, 2001).
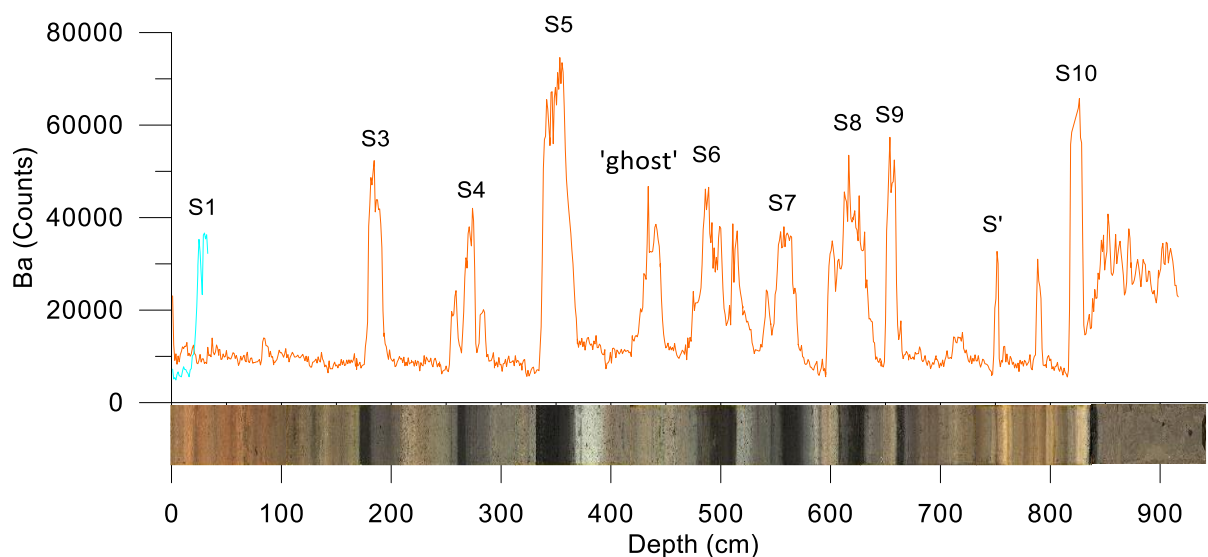

Figure 2 | XRF scanning record of Barium. Barium is regarded as a good proxy for export productivity.

3 Materials and methods

3.1 Core material and sampling

Piston core 64PE406-station 1 (33° 18.14898' N, 33° 23.71998' E; 1760 m water depth, total core length of 9.6 m) has been retrieved during the East Mediterranean NESSC (Netherlands Earth System Science Centre) cruise. In this study, we investigated the first 845.5 cm of the core covering the ~350 cal ka BP. Ten sapropel layers (S1, S3, S4, S5, S6, S7, S8, S9, S' and S10) have been identified in core 64PE406 based on a X-ray fluorencence (XRF) core scanning record of Barium (Ba) (Figure 2). Barium is enriched in sapropels, being a proxy of export productivity (Thomson et al., 1995; de Lange et al., 2008), and therefore ideal to identify sapropels, even if post-depositional diagenesis occurred (Thomson et al., 1995; Santvoort et al., 1996; de Lange et al., 2008). Sediment core 64PE406-E1 was split in an archive and work half with a core slicer, and the archive half was sampled each centimetre. The sediment samples were weighed directly after sampling and freeze-dried to remove all water.

After drying the samples were weighted again to determine the concentration (in weight percentage) of water in each sample (Figure 3).
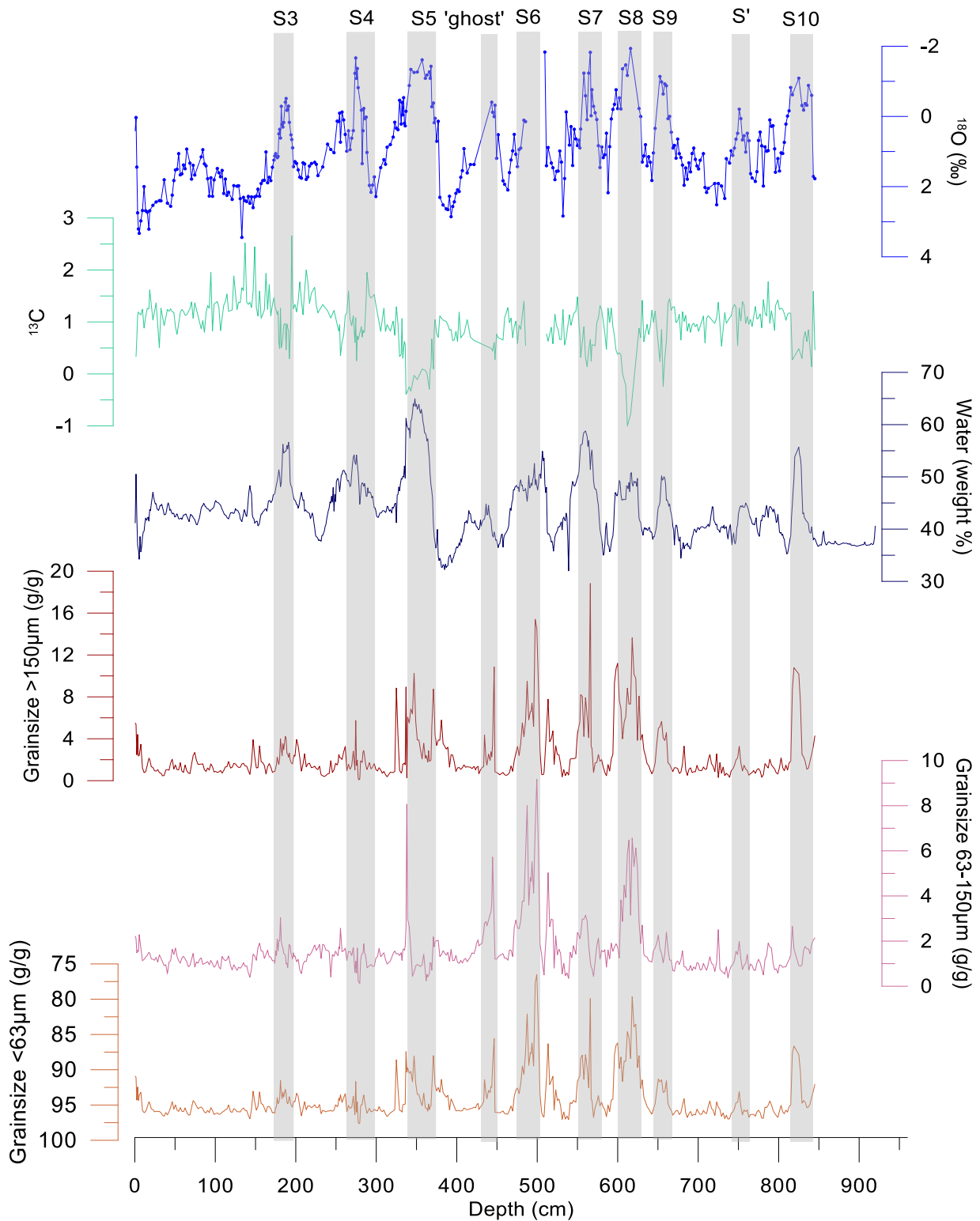

Figure 3 | Oxygen isotope, calcite, water content and grain-size fractions record for piston core 64PE406-E1 plotted against depth. Note that the water content are reported in weight % and grain-size as >150 μm, 63-150 μm and <63 μm (g/g). Grey bars indicate sapropel layers. Sapropel layer S1 is absent in the piston core.

3.2 Sample preparation for geochemical analyses

The core was analysed at a 2 cm interval for Mg/Ca, Na/Ca, Ba/Ca and isotope composition (δ^{18}O) in shells of *G. ruber* (white) specimens. Some key intervals were analysed at a higher resolution (every 1 cm), to cover the initiation and termination of the sapropels. The sediment samples were wet sieved over Endecott stainless-steel sieves, with mesh sizes of 63 and 150 µm, and subsequently dried at 60°C overnight. The dried fractions were weighed again to determine the amount of particles within these size fractions (Figure 3) and dry-sieved over 63, 250 and 355 µm sieves. The 250-355 µm fraction was split in a working and archive split. Between 30 and 40 specimens of *G. ruber* were picked in each sample from the 250 – 355 µm fraction, thereby avoiding specimens that appeared contaminated, heavily encrusted or showed signs of diagenesis. Representative specimens from different depths of the core, both sapropel and non-sapropel samples, were selected for a closer examination of the calcite shell quality, using a tabletop Hitachi TM3000 Scanning Electron Microscope. This provided more insight on crust formation and diagenesis of the calcite shells, and differences therein between sapropel and non-sapropel specimen. *G. ruber* (white) was reasonably abundant throughout the core, except for one interval 487.5 – 508.5 cm (~167-179 ka), were *G. Ruber* was absent. Abundances were low within the intervals around 426.5 – 443.5 cm (~140-143 ka) and 277.5 – 279.5 cm (~108 ka), 337 – 338 cm (~122 ka) and 622.5 – 624.5 cm (~218 ka), and ~10-15 specimens were picked.

Prior to analysis, foraminifera were cleaned using an adjusted Barker protocol (Barker et al., 2003, modified by Cambridge and NIOZ). Firstly, foraminiferal shells were gently crushed between two glass plates, in order to remove contamination such as clays and coccoliths, present inside the shells, during subsequent cleaning steps (Boyle and Keigwin, 1985). The crushed foraminifers were then transported to acid-leached 500 µl vials. Clays and coccoliths were removed using a *minimal settling technique*, by removing the supernatant containing the contamination with ultrapure Milli-Q$^+$ water and methanol, right after the heavier carbonate shell fragments are settles (~5 seconds). Organic matter was removed by oxidation, by adding an alkali buffered H_2O_2 solution to the shells and heating them for 10 minutes in an ultrasonic bath at 95 °C. NaOH was hereby replaced by NH_4OH in order to avoid contamination of the samples when measuring Na/Ca. The oxidizing reagent was removed by several rinses with ultrapure Milli-Q$^+$ water. For the oxygen isotope analysis, this was the final step of the cleaning protocol.

The samples for the solution-ICP-MS analysis were transferred to new acid-leached vials and required further cleaning steps for the removal of metal oxides and adsorbed ions. Diluted hydrazine hydroxide was added to each sample. The samples were placed in an ultrasonic bath with boiling ultrapure Milli-Q$^+$ water and were ultra-sonicated 2 seconds every 2 minutes, during 30 minutes. The supernatant solution was then removed with several rinses of cold and hot ultrapure Milli-Q$^+$ water. Finally, the samples were briefly leached with 0.001 M HNO_3 to further remove adsorbed ions from the foraminiferal shells.

3.3 Stable isotope analysis

In order to establish a stable oxygen isotope record, 387 samples were analysed using a Kiel-device (type ''Kiel IV'') coupled to a Thermo-Finnigan MAT253. Around 15-45 µg carbonate was used for stable oxygen isotope analyses. A standard run consisted of 38 samples interspersed with 5 in-house standards (NFHS-1) and 4 international carbonate standards (NBS-19). The isotope ratios are given relative to the Vienna Pee Dee Belemnite (VPDB) standard using the delta notation. Results were

normalized against NBS19 ($\delta^{18}O$ = -2.20‰, $\delta^{13}C$ = 1.95‰) and in-house standard NFHS-1 ($\delta^{18}O$ = 1.148‰, $\delta^{13}C$ = 0.854‰). The mean external reproducibility was better than ±0.05‰.

3.4 Solution-ICP-MS analysis

The cleaned foraminifera fragments were dissolved in 0.5ml 0.1 M HNO_3, ultra-sonicated for 15 minutes and centrifuged for 5 minutes to settle any remaining small silicate particles (although the Barker protocol (Barker et al., 2003) uses a silicate removal step, we also used centrifugation for the removal of silicate particles). The samples were transferred to trace-metal cleaned vials, leaving 30 µl of the solution behind to avoid contamination by the supernatant. In total 435 samples were measured. Trace element/Ca ratios were measured by ICP-MS at the Royal Netherlands Institute for Sea Research (NIOZ) using a SF-ICPMS (Thermo Fisher Scientific Element-2). Isotopes ^{23}Na, ^{24}Mg, ^{25}Mg, ^{27}Al, ^{43}Ca, ^{48}Ca, ^{55}Mn, ^{56}Fe, ^{88}Sr and ^{138}Ba were measured during 3 minutes. Six ratio calibration standards with similar matrix were used for optimal accuracy and precision of the instrument. After five samples a drift and monitor sample was measured. The samples were quality checked with monitor standards JCt1, JCp1 and in-house foraminifera standard (NFHS-1). Trace element/Ca ratio were calculated using matlab and were corrected for instrument and dissolution-acid blank.

Measurements with a ^{43}Ca ratios of <1e7 mmol/mol were excluded from further analysis because the Ca concentrations was too low for reliable elemental ratios. Foraminiferal Al/Ca, Fe/Ca and Mn/Ca were used to validate the cleaning efficiency of the procedure and contamination by clay minerals and diagenetic overgrowths (Barker et al., 2003; Pena et al., 2005; Weldeab et al., 2006; Elderfield et al., 2010). Clay minerals and diagenetic overgrowths that are still attached to the shells after cleaning may offset the analyses. Samples with high Al, Fe and Mn concentrations are therefore considered contaminated and were excluded from further analysis (Figure S1). Of all measured data, ~24 % was rejected because of too low ^{43}Ca concentration, contamination values for Al, Fe and Mn were too high or for having unrealistic Na ratios (>20 mmol/mol).

3.5 LA-ICP-MS and SEM analysis

To assess the impact of overgrowths on foraminiferal Mg/Ca ratios down-core, we selected ten intervals, covering the measured range of Mg/Ca values during sapropel and non-sapropel periods (3 - 12 mmol/mol Mg/Ca; Figure 3) for LA-ICP-MS and SEM analysis. Of each interval, ten specimens were picked and organic matter was removed using an oxidative cleaning step (see section 3.2). Prior to laser ablation, SEM images of a total of 37 *G. ruber* specimens were taken to assess the structure of the outer surface. The element concentrations of the last 1-3 chambers of each specimen were measured using La-ICP-MS (Reichart et al., 2003). The laser ablation system (NWR19UC, New Wave) consists of a ARF excimer laser with 193 nm pulse width. Each sample was targeted by a laser fluence of 1 (±0.05) J/cm^2 and at a repetition rate of 4 Hz. The laser ablated during 2 minutes a round spot with a diameter of 80 µm into the surface of the foraminifera shell. The ablated material was transported in a helium environment (0.7 L/min gas flow) to the ICP-MS (Thermo Scientific iCAP-Q) using a smoother that had been optimized for high sensitivity of ^{24}Mg and low ThO/Th ratios (< 1%).

3.6 Age model

The age-depth model for core 64PE406-E1 was established by comparing our $\delta^{18}O_{ruber}$ record with the well-dated Israeli speleothem oxygen isotope record of the Soreq cave (Grant et al., 2012) over

the interval 0-130 ka BP. The correlation was based on the fact that both the $\delta^{18}O_{ruber}$ and Soreq $\delta^{18}O_{speleothem}$ are impacted by $\delta^{18}O$ changes of Mediterranean surface waters. This correlation is justified, as the $\delta^{18}O$ of the Soreq cave mainly reflect the precipitation source (i.e. Mediterranean surface water, Grant et al., 2012) and therefore largely resemble the $\delta^{18}O$ of the Mediterranean seawater. The uncertainties of the oxygen isotope record of the Soreq cave (at 2σ) for the first 40 ka BP is 0.4±0.2 kyr and 2.0±0.9 kyr for the interval >40-150 ka BP (Grant et al., 2012; Grant et al., 2016). To establish the age model for the deeper part of our record we tuned the Ba/Al record of this core to the Ba/Al record of core ODP968 (Ziegler et al., 2010). The initial model of core OD968 is based on the sapropel midpoint age of Lourens (2004), colour reflectance at 550 nm, Ba/Al and Ti/Al records of the core OD968 linked to the Chinese speleothem oxygen isotope record of Sanbao and Hulu caves (Wang et al., 2008; Ziegler et al., 2010). This correlation is primarily based on the colour reflectance record of OD968 to the $\delta^{18}O$ of the Chinese caves, and assuming similar variability in monsoon intensity in China and Africa.

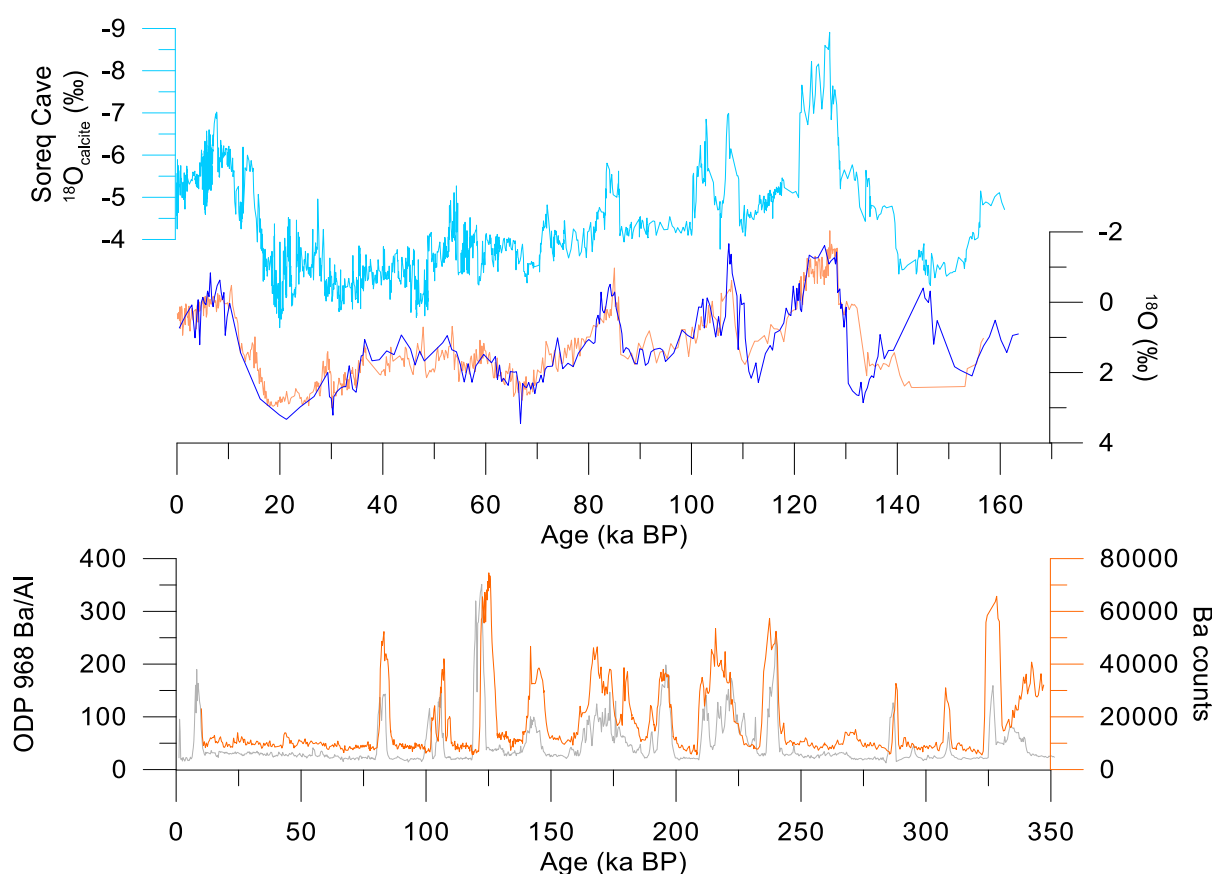**Figure 4 |** Oxygen isotope record of site 64PE406-E1 (blue) compared with the $\delta^{18}O_{ruber}$ of LC21 (light orange, Grant et al., 2012; 2016) and the Soreq cave speleothem $\delta^{18}O$ record (light blue, Grant et al., 2012). Barium record of core 64PE406-E1 compared with the Ba/Al record of ODP 968 (Ziegler et al., 2013).

3.7 SSS estimations

Sea surface salinity (SSS) was derived from our Mg/Ca record. The Mg/Ca ratios in the EMS appear to be strongly influenced by salinity and therefore Mg/Ca may partly reflect sea surface salinity changes over time. To this extend, we used existing sea surface temperature (SST) data based on $U_{37}^{k'}$ from the Western Mediterranean Sea (Iberian Margin) (Matras et al., 2007) and normalized it to the Late Holocene SST based $U_{37}^{k'}$ from the EMS (Castañeda et al., 2010). The normalized SST were converted

to sea surface salinity based on our Mg/Ca record using the *G. ruber* Mg/Ca-temperature equation of Kisakürek et al. (2008) (Mg/Ca = exp[(0.06±0.02) x SSS) + 0.08(±0.02) x SST - 2.8 (±1.0)]).

3.8 δ^{18}O residuals

Mediterranean seawater δ^{18}O is strongly influenced by sea-level variability due to the restricted exchange between the Atlantic Ocean and Mediterranean Sea during glacial periods (Rohling, 1999; Rohling et al., 2014). We use the δ^{18}O$_{ruber}$ record as a proxy for surface water freshening caused by the monsoon run-off, therefore it is important to remove the sea-level component from the δ^{18}O$_{ruber}$ record. First, we converted the Red Sea relative sea-level record into equivalent eastern Mediterranean δ^{18}O values based on the upper and lower probability limits for a quadratic relationship between Mediterranean δ^{18}O and sea-level published in Rohling et al. (2014). The converted Red Sea sea-level record was normalized to the Late Holocene values δ^{18}O$_{ruber}$ values and then subtracted from δ^{18}O$_{ruber}$ record. Then, we calculated the δ^{18}O$_{residuals}$ by subtracted the upper/lower 95% probability intervals of the converted Red Sea sea-level record from the δ^{18}O$_{ruber}$.

4 Results

4.1 Grainsize and water content

The concentrations (in weight percentage) of water and grain-size fractions of each sample are plotted versus depth in Figure 3. Water concentrations vary between 30 to 65%. The concentration of water in each sample shows systematically abrupt and large amplitude changes during sapropels. The water content in sapropelic layers is generally more than 50% while sediments from non-sapropel periods contain 30% water. The grain-size data show finer-grained intervals during non-sapropel times and coarser-grained intervals occur during sapropels. The coarse grain-size intervals occur in S6 and S8.

4.2 Oxygen isotope record

G. ruber δ^{18}O values show negative excursions in all ten late Quaternary sapropel layers (Figure 3). There are a few small gaps in the δ^{18}O record due to low abundance or complete absence of *G. ruber* during these intervals. The largest gap occurred within sapropel layer S6. Carbon Isotope values show large variations ranging from 3.33 ‰ to -1.935‰ (Figure 3). The δ^{18}O of *G. ruber* are marked by very low values (up to -1.66‰) during sapropels and higher δ^{18}O values (2‰) during non-sapropel periods. The maximum glacial-interglacial amplitude of *G. ruber* is from ~2.8‰ to ~-1.43‰ at ~128 ka BP.

4.3 Solution ICP-MS

G. ruber Element/Calcium (El/Ca) values are correlated to the occurrence of sapropels (Figure 5). The Ba/Ca ratios range from 0.7 to 118 µmol/mol and show increased values in most of the sapropels, most notably in sapropels of the top 200 ka of our record (S1-S7). The Ba/Ca$_{ruber}$ in sapropels are characterized by high values (up to 77 µmol/mol), with the exception for interval 204 to 252 ka BP, compared to non-sapropels times (~1 µmol/mol). Generally, the Ba/Ca ratios show a sharp increase at the sapropel onset followed by a gradual decrease towards the sapropel termination (Figure 5). The most pronounced and abrupt shift in Ba/Ca ratios occurred at the onset of sapropel S5 (from 2 to

77 µmol/mol) followed by a more gradual decline. Furthermore, elevated Ba/Ca ratios are also found in between sapropels around 67 ka and 227 ka.

The most striking feature in the Mg/Ca$_{ruber}$ record is the gradual increase and decrease of Mg/Ca, which is anti-correlated to sapropels. Hence, Mg/Ca ratios reach peak values in between sapropel periods (~13 mmol/mol) and decrease to valleys of low Mg/Ca (~3 mmol/mol) during sapropel intervals.

Although Na/Ca values show relatively large variability (6 – 20 mmol/mol), the Na/Ca record does systematically show higher Na/Ca ratios in sapropels, except for S8 and S9. The Na/Ca values are highly scattered from ~300 ka BP and show no systematically relationship to the occurrence of sapropel and non-sapropel periods.

The Sr/Ca ratios show less variability, ranging from 1.4 – 1.6 mmol/mol. The Sr/Ca ratio shows an increasing trend down-core. There are no major differences between sapropel and non-sapropel periods.
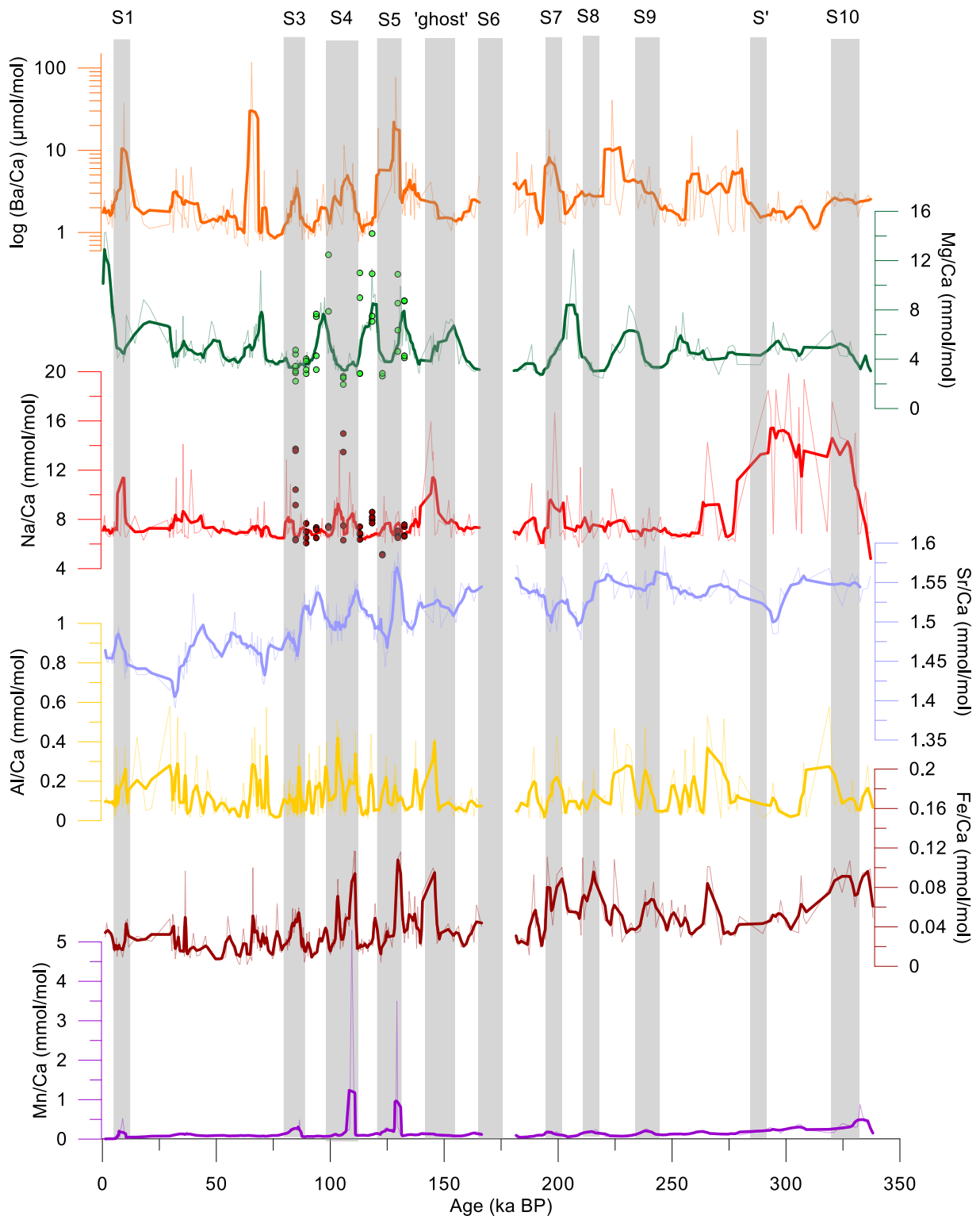
Figure 5 | Trace element ratio based on shells of planktic foraminifera *G. ruber* (250 to 350 μm) from core 64PE406-E1 plotted versus calendar age (ka BP). The Mg/Ca and Na/Ca values obtained with LA-ICP-MS are shown in green and red dots. Grey bars indicate sapropel layers.

4.4 Elemental distribution within the foraminiferal shell

SEM images of *G. ruber* show different degrees of crust formation between sapropels and non-sapropels from interglacial MIS 4, whereby sapropel specimens show high levels of overgrowths and non-sapropel samples show less crust formation (Figure 7). This difference in shell morphology is reflected in the Mg/Ca values obtained with solution-ICP-MS. To better assess the nature of these

differences in elemental composition and its relationship to overgrowths and diagenesis we obtained La-ICP-MS profiles. LA-ICP-MS element depth profiles allow comparison of the intra-shell Mg/Ca distributions between sapropels and non-sapropels specimens. Profiles show low Mg/Ca in sapropel specimen versus high Mg/Ca peaks at the outside of the shell in non-sapropel specimen (Figure 8 and S2).
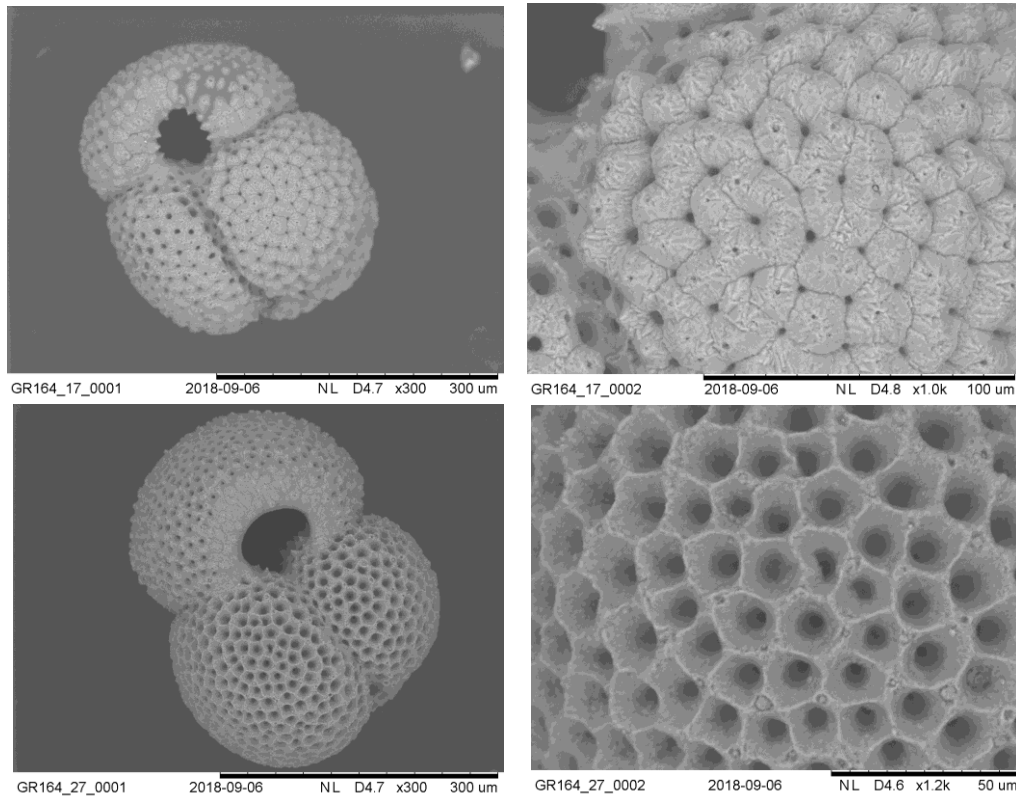

Figure 6 | Representative SEM images of *G. ruber* specimens from Sapropel (upper) and non-Sapropel (lower) periods. The SEM images reveal heavy crust formation in the Sapropel specimen, showing low Mg/Ca values, and no signs of crust formation of the non-Sapropel specimen, showing high Mg/Ca values.
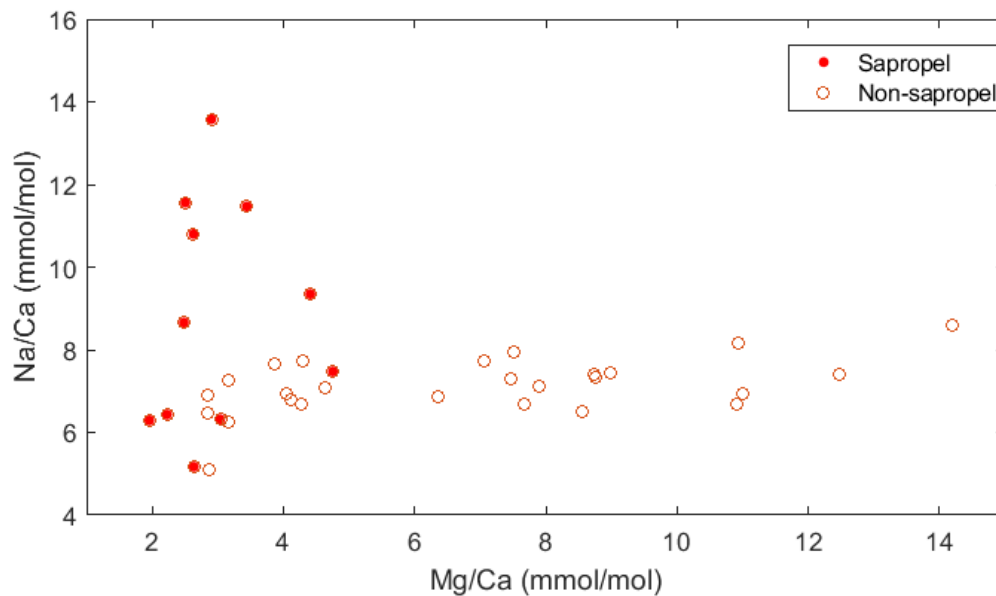

Figure 7 | Na/Ca versus Mg/Ca values obtained with LA-ICP-MS for sapropel and non-sapropel samples. Note the higher Na/Ca and lower Mg/Ca values for sapropels compared to non-sapropels.

5   Discussion

5.1   Sea surface temperature proxies

5.1.1 Mg/Ca

The Mg/Ca paleo-thermometer is a well-established proxy for SST estimations. Foraminiferal Mg/Ca in foraminiferal calcite has been shown to be mainly controlled by calcification temperature (Lea et al., 1999; Dekens et al., 2002; Anand et al., 2003; Ferguson et al., 2008), whereby more Mg is incorporated at higher temperatures. However, Mg/Ca has also been shown to depend on the seawater Mg/Ca ratio (Evans et al., 2012). Furthermore, Mg/Ca can potentially be used to correct foraminiferal $\delta^{18}O$ for the SST effect, in order to obtain the salinity-related $\delta^{18}O$ (Rohling and Bigg, 1998). However, it has been shown that in high salinity environments (> 36 psu), such as the EMS, overgrowth of non-biogenic calcite affects the foraminiferal Mg/Ca ratio (Hoogakker et al., 2009; Kontakiotis et al., 2011; 2017) and the reliability of this proxy in high salinity conditions has therefore been questioned. The Mg/Ca ratios in planktic foraminifera *G. ruber* in our record show relatively high Mg/Ca ratios (up to ~13 mmol/mol), especially during non-sapropel periods (Figure 5, 8c), yet these high values are typical for the eastern Mediterranean Sea. Measured foraminiferal Al/Ca and Fe/Ca ratios rule out that these high Mg/Ca values are caused by contamination of clay minerals.

Interestingly, SEM images show signs of heavily overgrowth during sapropel times, while overgrowths appear less frequently during non-sapropel periods. The visually highly overgrown specimens generally lower Mg/Ca values (> 2.5 – 3 mmol/mol) than those that show no sign of overgrowth (up to 12.92 mmol/mol). Laser ablation depth profiles of *G. ruber* shells show a peak in Mg/Ca at the outer shell of highly overgrown specimens (Figure S2). However, the observed high Mg/Ca cannot be explained by overgrowth or the dependence of Mg/Ca on temperature. Kisakürek et al. (2008) showed that salinity has a strong effect on Mg/Ca in cultured *G. ruber*, which is also observed in the EMS (Ferguson et al., 2008). We have also compared our results with those obtained by Mezger et al. (2016) from the Red Sea (Figure 9a). The Mg/Ca values of our core are lower compared to the Mg/Ca values from the Red Sea, another high-salinity basin, especially for the sapropels, suggesting less saline conditions during sapropels, which is in line with previous observations (e.g., Rossignol-Strick et al., 1982). It seems, therefore, that the high Mg/Ca values in our core can be attributed to SSS bias. However, during sapropels, Mg/Ca values reach more 'expected' levels of less saline conditions, however the Mg/Ca derived temperature estimate appears to be biased by the low Mg/Ca overgrowth (Steinhardt et al., 2015). These complications make it impossible to apply the Mg/Ca paleothermometer to the entire record. However our sapropel specimens show Mg/Ca derived SST's of ~26°C, which is lower than the present-day temperature. This may indicate that the Mg/Ca derived temperature estimations in sapropel specimens appears to be biased towards lower temperature values by the low Mg/Ca overgrowth (Steinhardt et al., 2015). These complications make it impossible to apply the Mg/Ca paleothermometer to the entire record. Further research should investigate the influence of salinity and low Mg/Ca crust on Mg/Ca-based temperatures in the EMS.
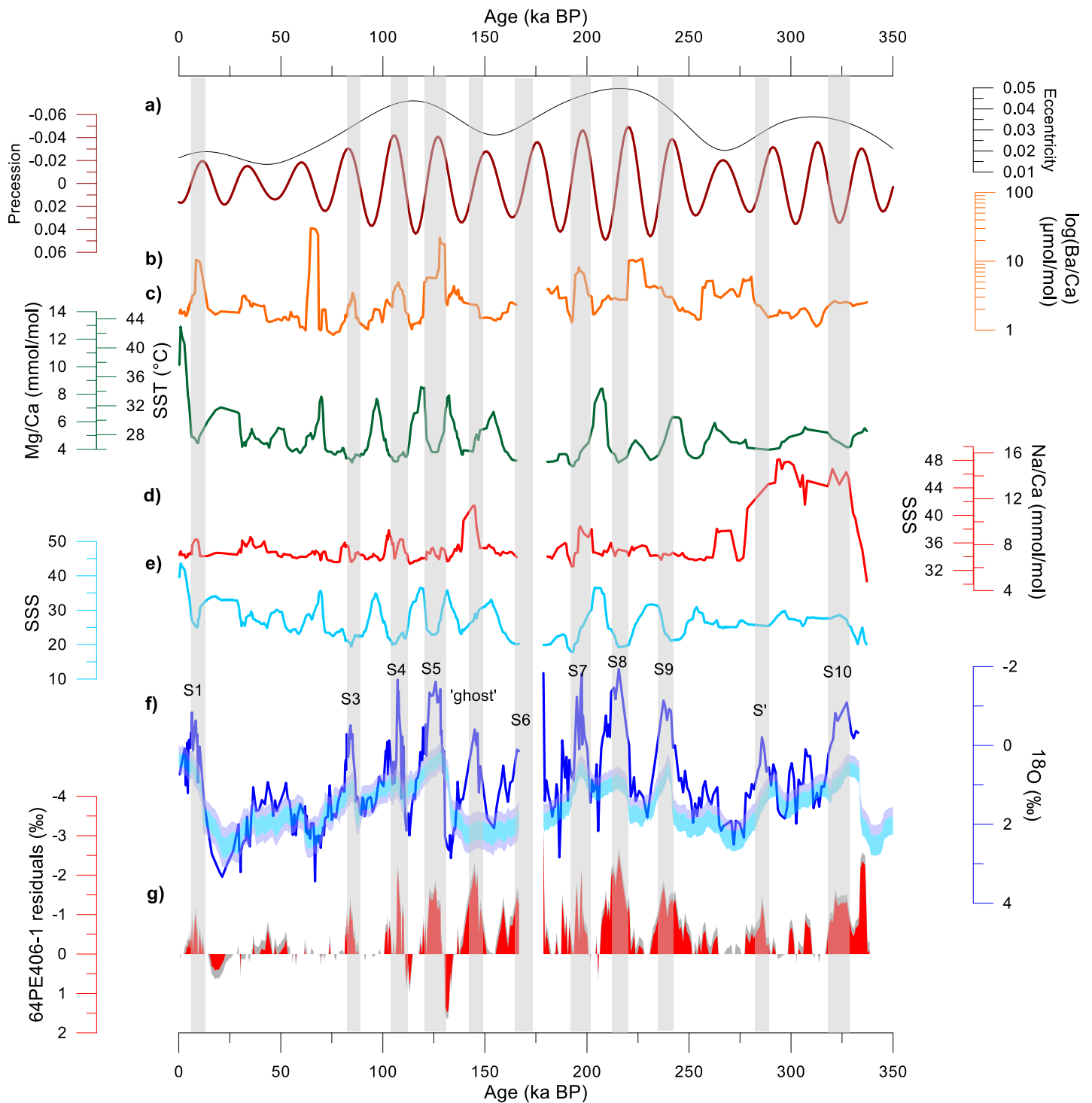
Figure 8 | Earth's orbital parameters (a) eccentricity (black) and precession (red) (Laskar et al., 1990). Time series of Ba/Ca (b), Mg/Ca (c) and Na/Ca (d). (e) Mg/Ca and U_{37}^k based SSS estimations. (f) Oxygen isotope record (blue), maximum (dark blue) and minimum (light blue) probability sea-level in equivalent Mediterranean δ18O values based on the Red Sea sea-level reconstruction of Rohling et al. (2014). (g) δ18O residuals beyond the 68% (red) and 95% (dark grey) confidence limits. Grey bars indicate sapropel layers.

5.2   Sea surface salinity proxies

Seawater salinity is an important parameter for studying past changes in the Mediterranean climate system. Seawater salinity in the EMS is influenced by monsoonal-fueled freshwater input, global ice-volume and the balance between evaporation and precipitation. We here aimed for several

approaches to reconstruct seawater salinity, using Na/Ca and residual δ^{18}O as direct SSS proxies. Ultimately our aim was to deconvolve δ^{18}O, Mg/Ca and Na/Ca, and hence potentially correct for the impact of salinity on SST proxies. Therefore we analyzed the calcite chemistry of *G. ruber*, a surface dwelling species, that lives in the upper 50m of the water column, mainly during late summer (Gonzalez-mora et al., 2008; Grazzini et al., 1990; Pujol and Grazzini, 1995), and can adjust to lower salinities (e.g., Schmuker and Schiebel, 2002). This species hence potentially reflects changing salinity conditions at the seawater surface, associated to sapropel formations and terminations. Below we discuss the outcome of each approach, including pitfalls and problems of each salinity proxy.

5.2.1 Ba/Ca

Temporal variability in Ba/Ca in *G. ruber* shells are used as a qualitative proxy for monsoonal fuelled run-off into the EMS, because an equation for past run-off SSS for the EMS is not established yet. River run-off and salinity are inversely correlated and seawater Ba concentrations are strongly influenced by riverine run-off. The concentration of dissolved Ba in tropical rivers, such as the Nile River, are primarily controlled by the amount of river run-off (Bahr et al., 2013). The uptake of Ba in planktic foraminiferal calcite linearly varies with Ba concentration in seawater and is independent of temperature and salinity changes (Bahr et al., 2013; Hönisch et al., 2011; Lea and Spero, 1994). Therefore, temporal variations provide valuable insights in run-off induced SSS variations. However, the use of Ba/Ca is restricted to regions that are affected by large freshwater influx.

In general, Ba/Ca values follows the δ^{18}O signal, but is less pronounced, suggesting that the Ba/Ca in foraminifera shells is, at least partially, controlled by river run-off (Figure 8b). Nile River run-off predominately controls the past variability of Ba/Ca in the EMS (Weldeab et al., 2015). Therefore, our Ba/Ca record primarily reflects changes in surface water freshening due to Nile River run-off. Furthermore, Ba/Ca can also be used to reconstruct African monsoon variability over the Nile basin. It is unlikely that other freshwater input, into the EMS transported significant amounts of dissolved Ba to the core site given the absence of large river systems along the Israeli coast. The Ba/Ca record shows peaks that coincide with sapropel onsets for S1 to S7, except for S8-S10, suggesting that enhanced Nile River run-off into the EMS is associated with the formation of these sapropels. The record shows relatively low Nile River run-off during weakened North African monsoon system and gradual transition to relatively high Nile River run-off during intensified monsoon system for sapropels S1, S3, S4 and S7. Similar observations have been made by Weldeab et al. (2015) for sapropel S1. However, the high peak in Nile River run-off at ~60 ka suggested by Ba/Ca is not related to sapropel formation or intensification of the monsoon system. This may reflect some threshold behaviour.
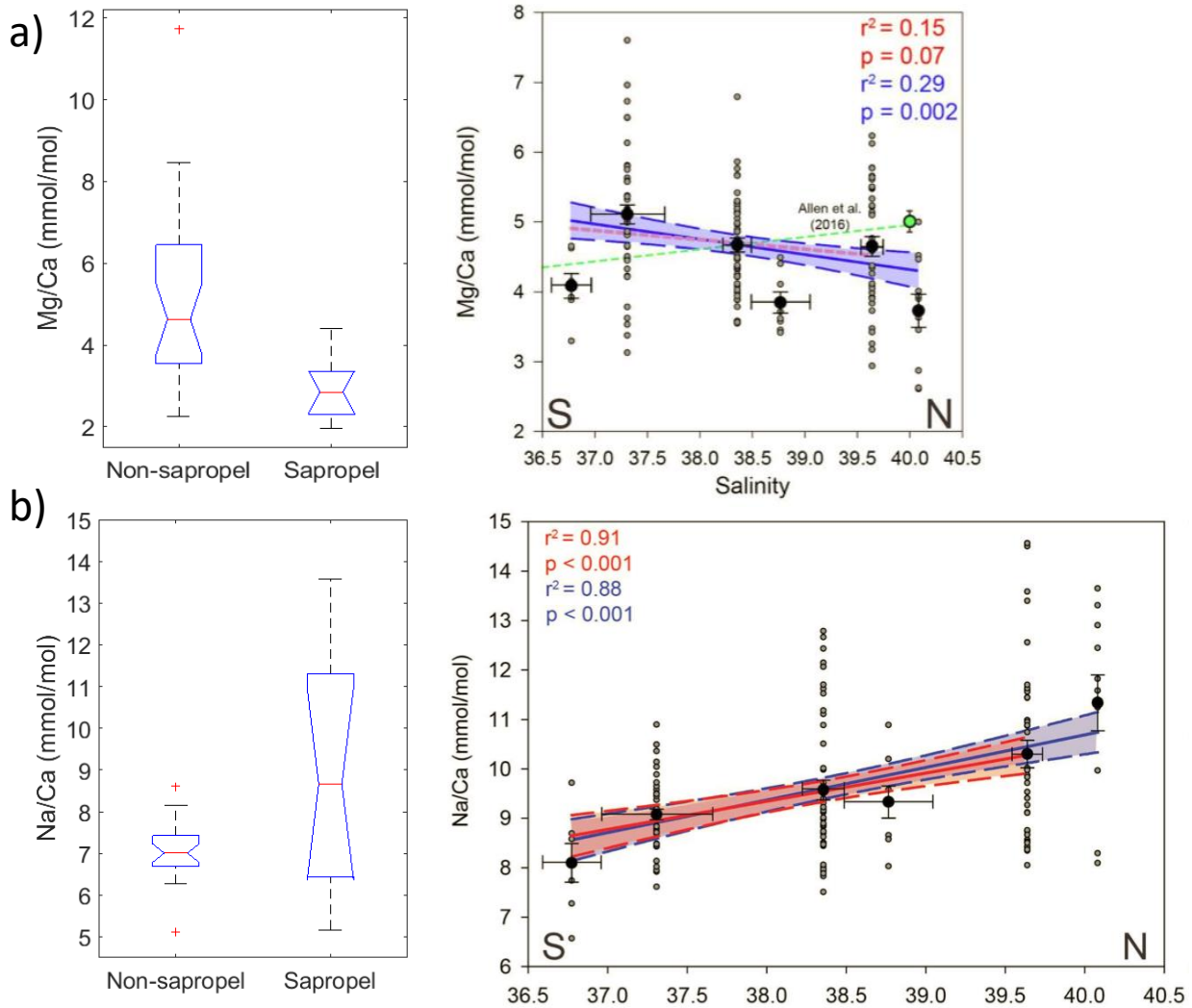
Figure 9 | Boxplots show Na/Ca and Mg/Ca values for *G. ruber* during sapropels and non-sapropel compared with the Na/Ca and Mg/Ca values from Mezger et al. (2016) for *G. ruber* test in the 129-353 µm size fraction from the Red Sea.

5.2.2 Na/Ca

The Na/Ca ratio in *G. ruber* shells has been shown to be positively correlated to seawater salinity in cultured and water-column specimens (Wit et al., 2013, Mezger et al., 2016). Here we aim to apply Na/Ca down core to assess if a Na/Ca derived salinity signal, related to monsoon variability in the EMS, is preserved in the sediment. In theory, Na/Ca can be used to correct for the salinity effect on *G. ruber* δ^{18}O. However, our Na/Ca results show an opposite trend than would be expected based on previous culture and plankton pump studies (Allen et al., 2016; Mezger et al., 2016) as Na/Ca levels are elevated during sapropels (Figure 8d). It has been shown that additional freshwater input from the Nile River created a freshwater lens in the EMS during sapropels (e.g., Rohling et al., 2015). Given that *G. ruber* lives at the surface, therefore, we would have expected lower Na/Ca values during sapropels. Applying our Na/Ca record as a proxy for SSS would hence result in more saline conditions during S1, S3, S7, S8 and S', compared to non-sapropels. Applying the Na/Ca salinity calibration of Mezger et al. (2016) results in salinities varying between 33 and 47. Thereby, the Na/Ca derived SSS of 33-35 for non-sapropels is lower than the present-day SSS of 39-41 (Figure 9). Therefore, Na/Ca

values in our record do not appear to correctly reflect salinity, since values would result in under-estimations of the salinity during non-sapropel periods.

When comparing our Na/Ca values with values obtained in Mezger et al. (2016), who assessed the relationship between foraminiferal Na/Ca and salinity on living foraminifera from Red Sea surface waters, we see that both the average and variability within sapropel Na/Ca values are comparable to Na/Ca values obtained in living specimens (Figure 10b). It hence appears that the relatively high inter-specimen variability in Na/Ca observed in foraminiferal calcite (Geerken et al., 2018), as well as the Na/Ca signal itself is only preserved in the sapropel layers, whereas Na appears to diffuse/leach from the calcite lattice in non-sapropel periods. This is corroborated by a recent study showing that foraminiferal Na, even though (partially) structurally bound, is leached from the calcite during burial, due to diagenetic processes (Yoshimura et al., 2017). Mezger et al. (2018) suggested that part of the high Na/Ca variability and signal in living $G.$ $ruber$ can be attributed to the presence of spines, which are enriched in Na/Ca, whereas these are lost in core-tops, resulting in lower Na/Ca values and loss of the salinity signal. It has also been suggested that Na is adsorbed to the organic template upon which calcification occurs, which might be oxidised and altered over time, hence also leading to a decrease in the Na-signal and variability down core (Branson et al., 2016). Possibly, all three mechanisms are involved and can explain the low Na/Ca values in non-sapropel periods. The 'normal' Na/Ca values during sapropels suggests that somehow the Na/Ca signal and variability are better preserved during anoxic conditions, preventing oxidation of the organic matrix and leaching of Na. Although further research should further investigate these mechanism, we might -with caution- attempt to use Na/Ca-derived SSS values to estimate salinity variability during sapropels. Using the salinity calibration of Mezger et al. (2016) Na/Ca during sapropels results in values of ~36.

5.2.3 Oxygen isotopes

Currently, oxygen isotope values have been used, after accounting for temperature and ice-volume effects from the $\delta^{18}O$ signal, to estimate past salinity (Rohling and Bigg, 1998). Paleotemperature estimations from foraminiferal Mg/Ca can be used to isolate these effects from the $\delta^{18}O$ signal. As mentioned in section 5.1.1, we cannot apply the Mg/Ca paleothermometer to our EMS specimens. One of the assumptions made by $\delta^{18}O$ based SSS estimations is that the relationship between seawater oxygen isotopes and salinity is assumed to be constant, however this relationship likely varied over the past due to spatial and temporal variability of water fluxes and their isotopic composition (Rohling and Bigg, 1998).

Foraminiferal $\delta^{18}O$ is strongly influenced by the isotopic composition and temperature of seawater. The oxygen-isotope composition of seawater is affected by addition of freshwater via precipitation or river run-off. Freshwater derived from heavy monsoon precipitation is distinctly depleted in $\delta^{18}O$ values compared to seawater (e.g. Rodrigues et al., 2000; Beuning et al., 2000). Mixture of monsoonal fuelled freshwater and Mediterranean surface waters causes low $\delta^{18}O$ anomalies in surface-dwelling foraminiferal calcite (e.g. Vergnaud-Grazzini et al., 1977; Rohling et al., 2004). To validate that the record reflects the African monsoon run-off into the EMS we compare the $\delta^{18}O_{ruber}$ of core 64PE406-E1 with the $\delta^{18}O_{ruber}$ of core LC21 (Grant et al., 2012; 2016), MS21 (Hennekam et al., 2015; Zwiep et al., 2018) and MD04-71 (Weldeab et al., 2003) (Figure 10). The general trends in the $\delta^{18}O_{ruber}$ of core 64PE406-E1 are similar to those observed in the other cores. This supports that the record primarily reflects Nile River run-off caused by changes in the North African monsoon during precession minima, with a large sea-level imprint during the glacial intervals (e.g., Rohling, 1994, 1999). These records show an increase in monsoon strength during sapropels and weaker monsoon strength during non-sapropel times.
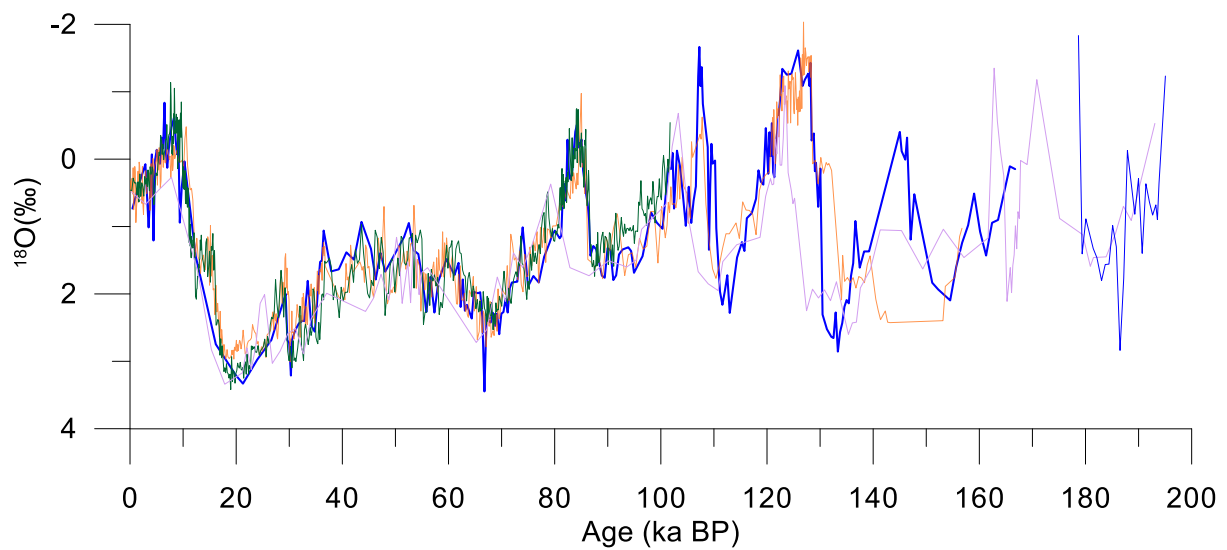
Figure 10 | Planktic foraminifera δ¹⁸O records from the EMS plotted against age (ka BP). The δ¹⁸O of this core in blue**,** LC-21 (Grant et al., 2012; 2016) in orange, MS-21 (Hennekam et al., 2015; Zwiep et al., 2018) in green and MD40-71 in purple (Weldeab et al., 2003).

The results show a correlation between the δ¹⁸O record and monsoon run-off but not or less for the trace elements. The observed differences could be due to (i) variable threshold responses among the different trace elements, (ii) overgrowth that effect elemental ratios, (ii) loss of trace elements due to dissolution of shell matter in deep sea sediment over time.

5.2.4   Multi-proxy approach

Even though Mg/Ca is traditionally not used as a SSS proxy, the Mg/Ca ratios in our record appear to be more influenced by salinity than SST. Our Mg/Ca record can be interpreted as a quantitative first order salinity estimation. This quantitative salinity reconstruction corroborates that the lowest salinity occurred during the sapropels (~20) (Figure 8e). However, the SSS estimations are lower than those based on Na/Ca (~36) (Figure 8d) and lower than previous salinity estimations for sapropel S5 by van der Meer et al. (2007), who suggest a salinity of ~33 at the onset of S5. This raises concerns about the reliability of a quantitative Mg/Ca-based SSS. We attribute these lower SSS values partly to the use of temperature equation of Kisakürek et al. (2008), which is based on cultured *G. ruber* and depend both on temperature and salinity. This is probably not a valid calibration for sapropels because the salinity effect on Mg/Ca is less during sapropel formation due fresh water lenses. Furthermore, the temperature in sapropels are also biased by low Mg/Ca crust (Steinhardt et al., 2015). We suggest that further studies are needed to better understand the influence of temperature and salinity on Mg/Ca of *G. ruber* under variable environmental conditions in the EMS, however, our SSS estimation can be used as a quantitative estimation salinity because it shows a clear precession-related signal.

5.3 North African monsoon variability and forcing

Comparison between the North African monsoon and the West African monsoon (core MD03-2707, Weldeab et al., 2007) over the last 150,000 years reveals very similar trends (Figure 11a). This view is supported by the Ba/Ca records of both cores. Temporal variability in Ba/Ca records from both cores

are assumed to reflect changes in riverine run-off and by extension changes in monsoonal strength and precipitation over the river basins. The moisture that fuels the monsoonal system originates mainly from the tropical Atlantic Ocean and the southern Indian Ocean (e.g., Gasse, 2000; Nicholson, 2009; Singarayer and Burrough, 2015), so discrepancies in the timing of river run-off may reflect different dynamics in moisture sources of the West and North African monsoon precipitation.

Precipitation over east Africa are mainly fed by the western Indian Ocean-sourced moisture (Costa et al., 2014). The earlier peak in monsoon fuelled intensification of precipitation in North Africa at ~130 ka BP reflects the dominance of the Indian Ocean-sourced moisture during the glacial-interglacial transition (MIS 6/5), which seems to be supported by the monsoon run-off peaks of the Ba/Ca record. During this glacial-interglacial transition, the Northern Hemisphere warmed abruptly and our data suggest that summer monsoon strength in East Africa increased while the West African monsoon showed a delayed response of ~2.5 kyr, which could be partly explained by age uncertainties. This delayed response in West African monsoon precipitation may be explained by the impact of freshwater fluxes into the North Atlantic. Model simulations have shown that the moisture transport from the Atlantic Ocean to West Africa weakened in response to freshwater fluxes (Chang et al., 2008; Tjallingii et al., 2008; Kageyama et al., 2013) due to the reduced Atlantic meridional overturning circulation (AMOC) and a southward shift in the ITCZ (Chang et al., 2008). The delayed response suggest that the duration of freshwater fluxes due to melting ice-caps induce a lag in West African monsoon timing, which is consistent with Grant et al. (2016).
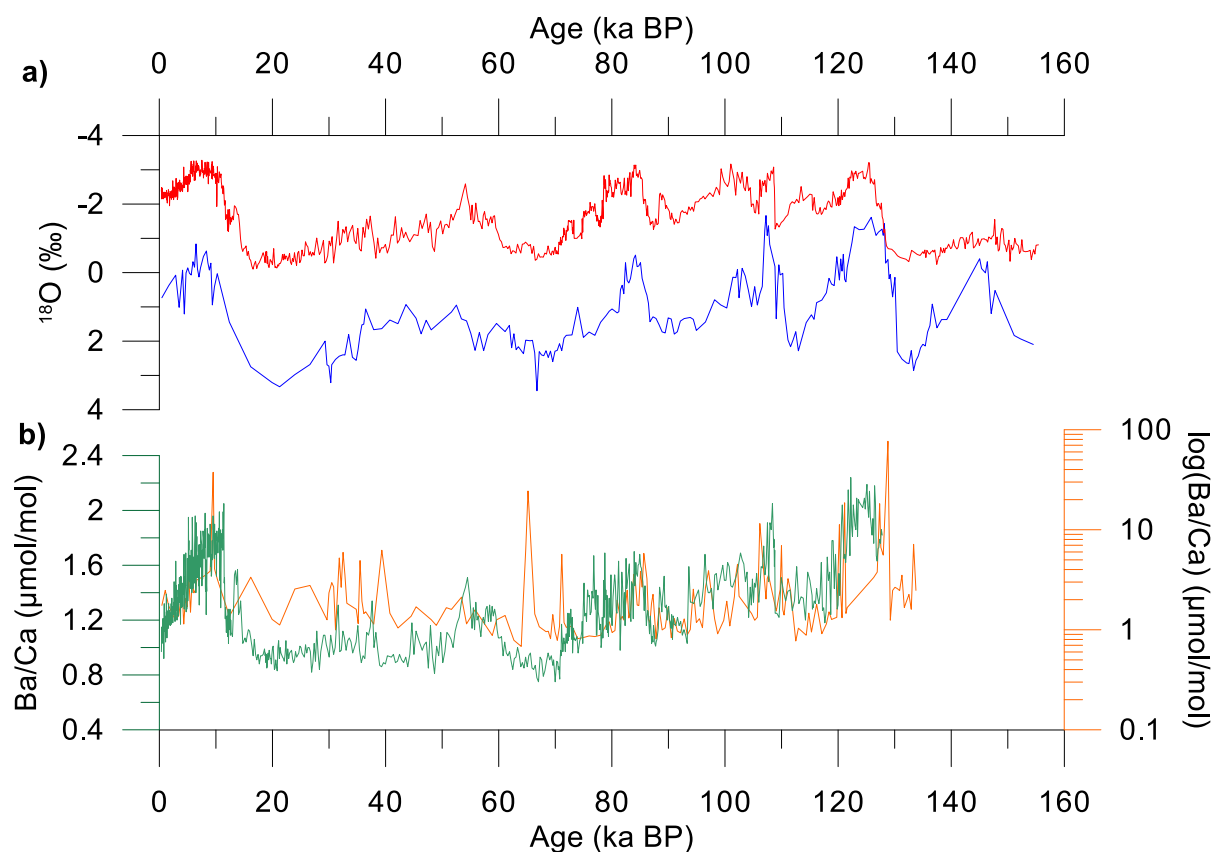

Figure 11 | Comparison between the North African and West African monsoons hydroclimates. (a) $\delta^{18}O$ data of core MD03-2707 (West African monsoon; Weldeab et al., 2007) in red and $\delta^{18}O$ data of core 64PE406-E1 (North African monsoon) in blue. (b) Estimate of riverine run-off in the Gulf of Guinea (green) and Nile River run-off (orange) based on Ba/Ca from *G. ruber* pink (core MD03-2707) and white (this study).

The most striking feature in the $\delta^{18}O$ record of the North and West African monsoon is the inverse trend around 145 ka BP (MIS 6). The $\delta^{18}O$ record of the West African monsoon indicates dry conditions while the $\delta^{18}O$ of the North African monsoon imply wet conditions, which is consistent with the $\delta^{18}O$ speleothem record of the Sanbao-Hulu cave (Wang et al., 2008; Cheng et al., 2016) (Figure 12). However, this record indicates a weak East Asian monsoon around this interval. Pollen records and model simulations show that the West African monsoon did intensify but was reduced in latitudinal extent due to weaker insolation maxima at that time (Davis and Brewer, 2009; Dalibard et al., 2014), i.e. monsoon rainfall didn't expand as far poleward at that time. The $\delta^{18}O$ of the ghost sapropel are less pronounced than for sapropels indicating a weaker monsoon system and associated Nile River run-off. This is somewhat supported by the $\delta^{18}O$ values of core LC21 and Soreq cave, which show no sign of elevated Nile River run-off around this time (Figure 4).

On orbital timescales, precipitation patterns between the north and south Africa are controlled by the position of the ITCZ and Congo Air Boundary. The ITCZ shift meridionally towards the hemisphere with the greatest radiative forcing resulting in an anti-phased relationship between North and South African precipitation (Simon et al., 2015). However, on millennial timescales the African climate is influenced by abrupt changes in the Northern Hemisphere (Heinrich events). Long proxy-based records of the North African monsoon shows that the African monsoon intensity was weakened during these events, which appears to be supported by the data (Figure 12). There appears to be a link between the weakening of the African monsoon intensity at Northern Hemisphere insolation maxima and more humid phases in South Africa during North Atlantic cold events (Ziegler et al., 2013). This bipolar seesaw behaviour is linked to the reduced AMOC strength and the more southward shift of the ITCZ (Broecker et al., 1998). The precipitation belt associated with the ITCZ likely shifted southward during North Atlantic cold events, but not very far south, which would lead to more humid conditions in South Africa (Simon et al., 2015).

Our $\delta^{18}O$ record also provides valuable insights in the palaeoenvironmental conditions for human dispersal and migration into Eurasia. Major migration events would have been possibly during humid intervals in North Africa that created favourable environmental conditions for survival of the human population and dispersal. Two major migration events into North Africa occurred around 128 ka (Petraglia et al., 2009) and 65 ka BP (Klein, 2000; Stringer, 2000; Mellars et al., 2006). Our record suggest modern human migration out of the sub-Sahara into North Africa around 128 ka BP would have been possible due to humid conditions in northern Africa (Figure 12). The second major migration event appears to fall within a period of dry conditions in northern African, which makes the migration out of the sub-Sahara less likely. However, the modern human populations show major expansion in Africa (Mellars et al., 2006). The residuals $\delta^{18}O$ seems to show more wetter periods between 60 and 32 ka BP (Figure 8), which in agreement with Viehberg et al. (2018) who suggested that during this interval modern human migration from the sub-Sahara was most successful. This is further supported by archaeological records and human dispersal models, which suggest a major human migration event during this period.
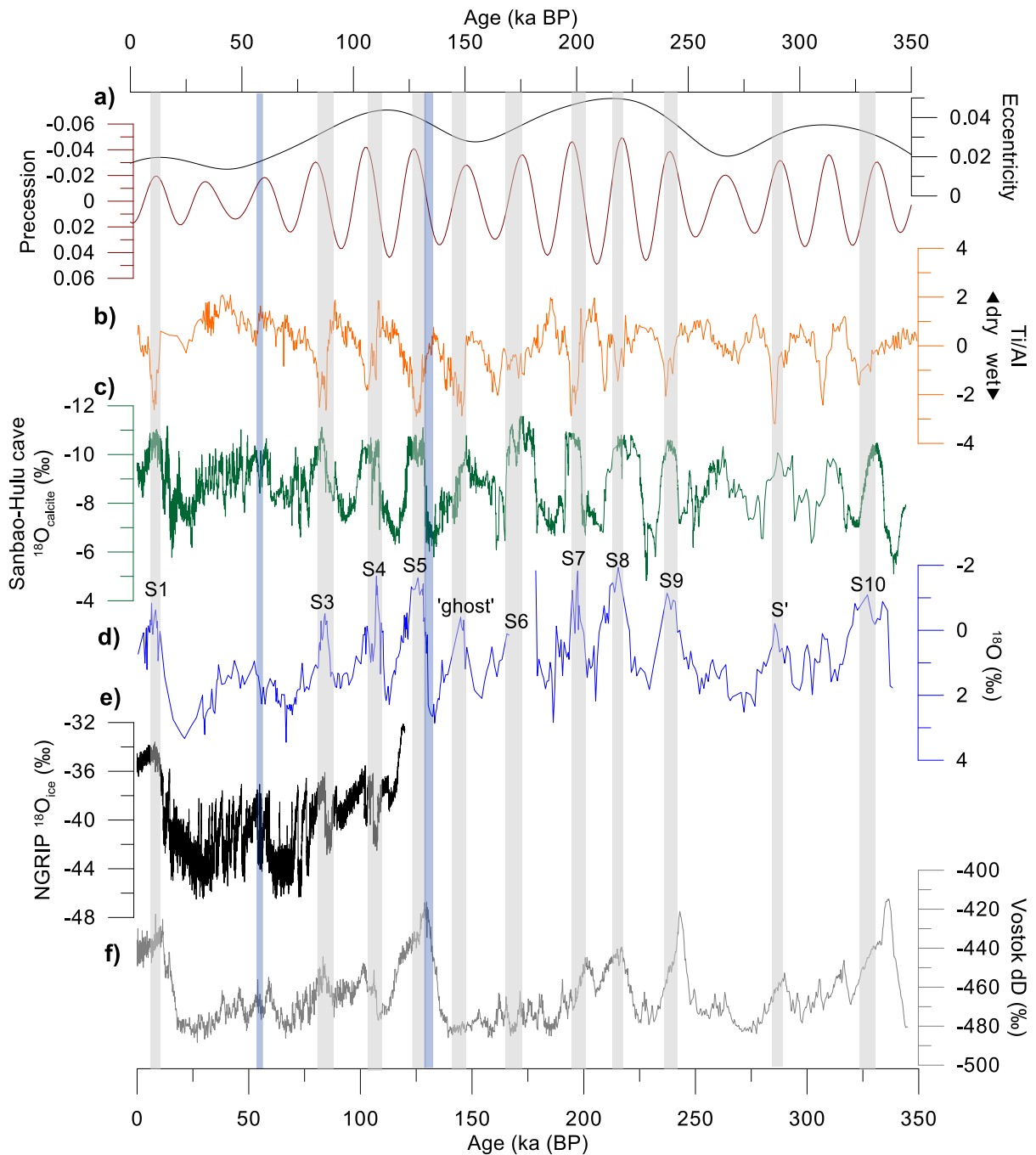
Figure 12 | Northeast African moisture variability over the past 350.000 years. Earth's orbital parameters (a) eccentricity (black) and precession (red) (Laskar et al., 1990), (b) Ti/Al, (c) speleothem δ¹⁸O Sanbao-Hulu cave (Wang et al., 2008; Cheng et al., 2016) showing variability in the East Asian Summer monsoon, (d) *G. ruber* δ¹⁸O record of core 64PE406-E1, (e) δ¹⁸O record from Greenland ice core NGRIP (Andersen et al., 2004) and (f) Vostok deuterium record (Augustin et al., 2004). Grey bars indicate sapropel layers and the blue bars indicate two major North African migration events.

5.4 Monsoon forcing and sapropel formation

Our reconstructions show that the increases in North African monsoon run-off coincide closely with the onset of sapropel depositions. This correlation in terms of timing suggests that monsoon-fuelled Nile River run-off is the primary driver for triggering surface buoyance changes for sapropel deposition, in correspondence with previous studies (Rohling et al., 2002, 2004, 2006; Emeis et al., 2003; Marino et al., 2007; de Lange et al., 2008; Hennekam et al., 2015; Grant et al., 2016). Our data also shows a link between North African monsoon run-off and anoxia intensity during sapropel

formation (Figure 13). However, model experiments for sapropel S1 showed that, in addition to monsoon forcing, the preconditioning for sapropel deposition was related to sea-level changes (Grimm et al., 2015). Comparable anoxia intensities were observed for S3, S4, S6, S7 and S8, and for S1, S9 and S10, which are deposited under a wide range of insolation forcing and sea-level trends, showing different responses under varying environmental/ climatic conditions.

The broadly similar $\delta^{18}O$ residuals and insolation values suggest that S3, S4, S6 and S7 were deposited during strong monsoon intensification (albeit less than sapropels S5 and S8) and low sea-level (Figure 5f,g and 13). The low sea-level reduced the exchange between the Atlantic Ocean and Mediterranean Sea, which may have increased the restriction of the basin, making it more susceptible to develop density stratification. This combined with increased nutrient input due to enhanced Nile River run-off would have fuelled production of organic matter and oxygen consumption in the deep layers, which leads to deep-water anoxia (e.g., Rohling et al., 2015). However, the deep-water anoxia responses are noticeably different for sapropels S3, S4 and S6 compared to S7. For sapropel S7, the anoxia response is a slowly developing trend whereas sapropel S3, S4 and S6 show rapid patterns of anoxia development. The modest Mo enrichments observed prior to S6 and S7 suggest weakening of the water column ventilation before the enhancement of surface water productivity (i.e., sediment Ba enrichment).

The maximum rate of anoxia strength is observed in S5. During S5, the African monsoon intensification coincides with a strong precession minimum and eccentricity maximum (Berger and Loutre, 1991) resulting in far more run-off than for the other sapropels. By contrast, the anoxia intensity during S3, S4, S6, S7 and S8 are roughly half the magnitude of S5. However, sapropels S5 and S8 have similar $\delta^{18}O$ residuals and corresponding insolation values, yet very different anoxia strength (Figure 13). Therefore, differences in anoxia strength for S5 and S8 are not simply explained by monsoon variability. The total sea-level change prior to S5 is tens of metres greater than for S8 (Figure 5), which may suggest a strong sea-level influence on deep-water anoxia to precondition S5. Alternatively, sapropel S8 was deposited during relatively cold 'glacial' conditions (Emeis et al., 2003), and the cold temperatures could have promoted ventilation, weakening the impacts of the strong monsoon and potential low sea- level.

The enrichment in Mo is less well defined for sapropels S1, S9 and S10, which were deposited at the end of major glacial terminations. The weaker anoxia intensity for S9 can be explained by falling sea-level. This is because falling sea-level would have reduced the exchange between the Atlantic Ocean and Mediterranean Sea, leading to increased SSS in the EMS, which in turn would have enhanced overturning and renewal of deep-water oxygen rather than stagnation (Grant et al., 2016). The relatively weak insolation maxima during S9 further support the role of sea-level, because weaker Nile River run-off has probably been insufficient for creating buoyancy forcing for deep-water stagnation. Sapropel S1 and S10 were deposited during less intense monsoon maxima. However, sea-level may have a strong influence on deep-water anoxia conditions, especially for sapropel S1 where sea-level continued to rise throughout S1 deposition. Rising sea-level would enhanced the exchange at the Strait of Gibraltar (e.g., Rohling, 1999; Rogerson et al., 2012) and combined with the inflow of low saline Atlantic water due to melting ice sheets, would cause stagnation of deep-water ventilation in the EMS (Rohling et al., 2015).

Our results show two types of responses: (1) a very rapid evolution of deep-water anoxia (sapropels S3, S4, S5, S6 and S8), and (2) a progressive evolution of deep-water anoxia (sapropels S1, S7, S9 and S10). To better understand the hydrological forcing leading to deep-water anoxia, we compare the $\delta^{18}O_{residuals}$ with the Mo record. The $\delta^{18}O_{residuals}$ of sapropels S1, S3, S4, S5, S7 and S9 reveal a rapid threshold response to forcing. This suggest that positive feedback mechanisms in relation to more

gradually changing environmental conditions lead to rapid anoxia during these sapropels (Figure 13). The onset of sapropels are marked by a more negative $\delta^{18}O$ and abrupt decrease in $\delta^{18}O$ (i.e., rapid strengthening of the monsoon) than at the end which marked by less depleted and more gradual $\delta^{18}O$ change (i.e., relatively modest –compared to onset- weakening of the monsoon). These results hint towards a so-called hysteresis response of anoxia to monsoon forcing.
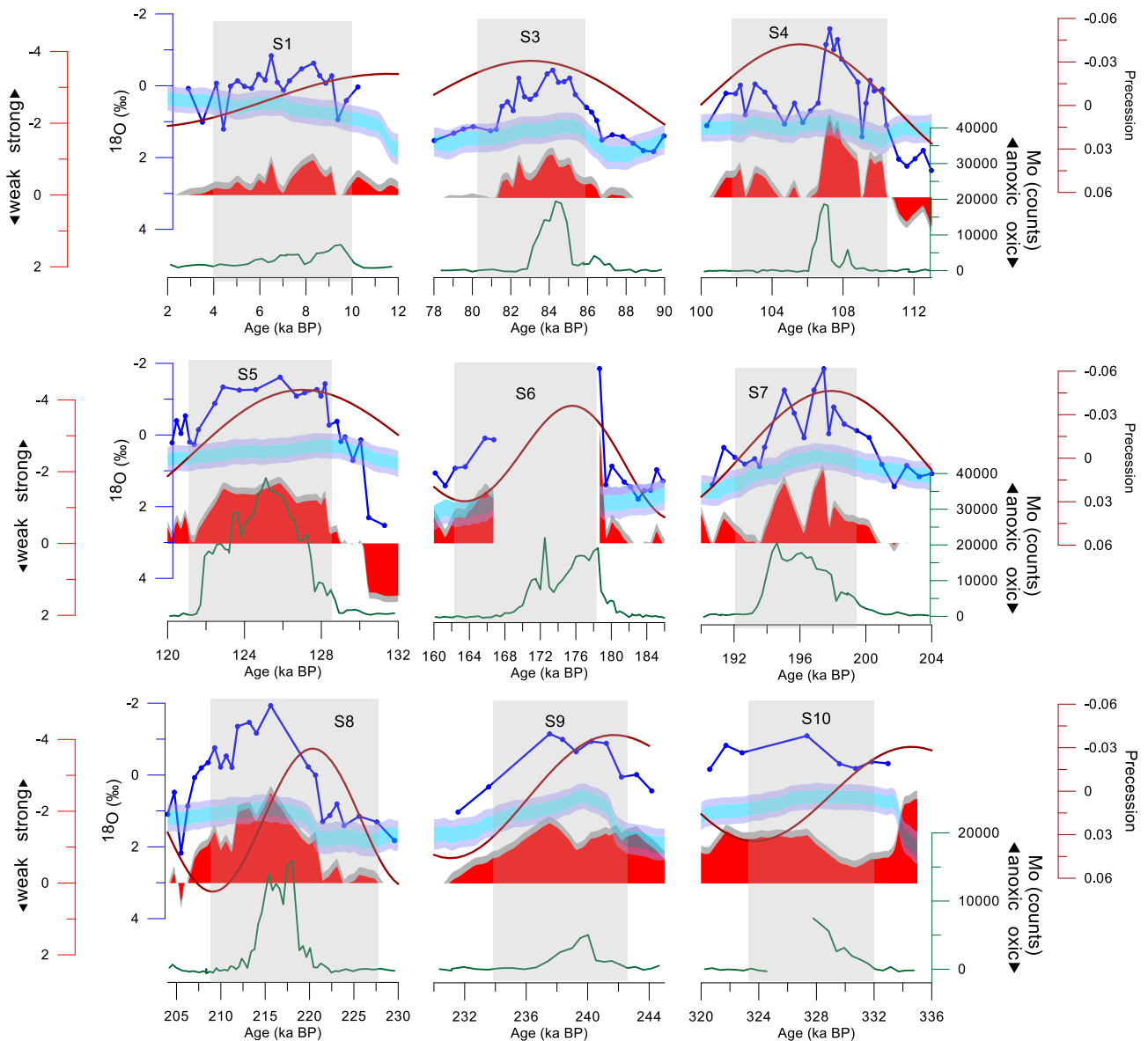

Figure 13 | Oxygen isotope, $\delta^{18}O$ residuals and redox sensitive (Mo) trace element plotted against age ka BP. Oxygen isotope record (blue), maximum (dark blue) and minimum (light blue) probability sea-level in equivalent Mediterranean $\delta^{18}O$ values based on the Red Sea sea-level reconstruction of Rohling et al. (2014). $\delta^{18}O$ residuals beyond the 68% (red) and 95% (dark grey) confidence limits. Sapropel boundaries (grey bars) are defined by Ba enrichments.

6   Conclusions

We examined a range of salinity proxies ($\delta^{18}O$, Ba/Ca, Na/Ca, and Mg/Ca) of the planktic foraminiferal species *G. ruber* from the eastern Mediterranean Sea of the last ~350 kyr. Our $\delta^{18}O_{ruber}$ and Ba/Ca primarily reflect Nile River run-off caused by changes in the North African monsoon while the other trace element ratios are more complex. The Mg/Ca record shows a strong precession-

related signal. The anomalously high Mg/Ca values that occur during non-sapropel time intervals, suggest a strong impact of salinity on the Mg/Ca values and excluding the use of Mg/Ca as a paleothermometer. However, our Mg/Ca-based SSS estimations can be used as a quantitative estimation, providing additional information on the environmental changes in the EMS over the studied period. The down-core Na/Ca record showed that Na is better preserved in the sedimentary organic layers (i.e., sapropels), which were deposited under anoxic conditions, whereas Na appears to diffuse/leach from the calcite lattice in non-sapropel periods. Ba/Ca values follows the $\delta^{18}O$ signal suggesting that Ba-enriched Nile River run-off controls the past variability of Ba/Ca in the EMS, at least during intervals with strong river runoff enhancements. The $\delta^{18}O$ record shows North African monsoon variability on multi to centennial time scales, especially when corrected for sea-level change effects. In general, the monsoon-fuelled intensification of rainfall in North Africa occurred somewhat earlier compared to the West African monsoon and more synchronous with Asian monsoon records. This implies that Indian-Ocean derived moisture was the dominant source for the North African monsoon during times of strong monsoon intensification, whereas today the Atlantic Ocean is the main source. This finding suggests that persistent meltwater pulses into the Atlantic Ocean, over several kyrs, influenced the timing of Atlantic Ocean moisture into West Africa, whereas Indian Ocean-derived moisture is more sensitive to orbitally forced changes in Northern Hemisphere summer insolation. The hydroclimatic changes over the Nile basin also influenced the human dispersal and migration into Eurasia. Our $\delta^{18}O$ and Ti/Al records show that around 128 and 60-32 ka BP wetter conditions would have made human migration into North Africa possible. Our $\delta^{18}O$ record also shows that monsoon forcing was the primary forcing mechanism for anoxia strength during sapropel formation, while sea-level and sea surface temperature can be considered a secondary forcing. However, for sapropels S1, S9 and S10 the sea-level effect may have been more important, which together with the relative weak monsoon intensifications at those times may explain the relatively weaker anoxia in comparison to other sapropels. Sapropels S3, S4, S5, S6 and S8 are characterized by a rapid evolution of deep-water anoxia whereas the evolution for sapropels S1, S7, S9 and S10 was progressive. There is no clear consistent trend in anoxia development under varying environmental/climatic conditions and forcings, suggesting a complex chain events leading to the varying anoxia intensities during sapropel intervals.

References

Adamson, D. A., Gasse, F., Street, F. A., & Williams, M. A. J. (1980). Late Quaternary history of the Nile. *Nature*, *288*(5786), 50.

Allen, K. A., Hönisch, B., Eggins, S. M., Haynes, L. L., Rosenthal, Y., & Yu, J. (2016). Trace element proxies for surface ocean conditions: A synthesis of culture calibrations with planktic foraminifera. *Geochimica et Cosmochimica Acta*, *193*, 197-221.

Anand, P., Ganssen, G., Elderfield, H., Peeters, F., Kroon, D., & Jung, S. (2003, December). Variability of Shell Mass, delta 18O and Mg/Ca in Planktonic Foraminifera: From Production to Preservation. In *AGU Fall Meeting Abstracts*.

Andersen, K. K., Azuma, N., Barnola, J. M., Bigler, M., Biscaye, P., Caillon, N., ... & Flückiger, J. (2004). High-resolution record of Northern Hemisphere climate extending into the last interglacial period. *Nature*, *431*(7005), 147.

Augustin, L., Barbante, C., Barnes, P. R., Barnola, J. M., Bigler, M., Castellano, E., ... & Dreyfus, G. (2004). Eight glacial cycles from an Antarctic ice core. *Nature*, *429*, 623-628.

Bahr, A., Schönfeld, J., Hoffmann, J., Voigt, S., Aurahs, R., Kucera, M., ... & Gerdes, A. (2013). Comparison of Ba/Ca and as freshwater proxies: A multi-species core-top study on planktonic foraminifera from the vicinity of the Orinoco River mouth. *Earth and Planetary Science Letters*, *383*, 45-57.

Barker, S., Greaves, M., & Elderfield, H. (2003). A study of cleaning procedures used for foraminiferal Mg/Ca paleothermometry. *Geochemistry, Geophysics, Geosystems*, *4*(9).

Beuning, K. R., Kelts, K., Russell, J., & Wolfe, B. B. (2002). Reassessment of Lake Victoria–Upper Nile River paleohydrology from oxygen isotope records of lake-sediment cellulose. *Geology*, *30*(6), 559-562.

Branson, O., Bonnin, E. A., Perea, D. E., Spero, H. J., Zhu, Z., Winters, M., ... & Gagnon, A. C. (2016). Nanometer-scale chemistry of a calcite biomineralization template: implications for skeletal composition and nucleation. *Proceedings of the National Academy of Sciences*, *113*(46), 12934-12939.

Broecker, W. S. (1998). Paleocean circulation during the last deglaciation: a bipolar seesaw?. *Paleoceanography*, *13*(2), 119-121.

Boyle, E. A., & Keigwin, L. D. (1985). Comparison of Atlantic and Pacific paleochemical records for the last 215,000 years: Changes in deep ocean circulation and chemical inventories. *Earth and Planetary Science Letters*, *76*(1-2), 135-150.

Castañeda, I. S., Schefuß, E., Pätzold, J., Damsté, J. S. S., Weldeab, S., & Schouten, S. (2010). Millennial-scale sea surface temperature changes in the eastern Mediterranean (Nile River Delta region) over the last 27,000 years. *Paleoceanography*, *25*(1).

Chang, P., Zhang, R., Hazeleger, W., Wen, C., Wan, X., Ji, L., ... & Seidel, H. (2008). Oceanic link between abrupt changes in the North Atlantic Ocean and the African monsoon. *Nature Geoscience*, *1*(7), 444.

Costa, K., Russell, J., Konecky, B., & Lamb, H. (2014). Isotopic reconstruction of the African Humid Period and Congo air boundary migration at Lake Tana, Ethiopia. *Quaternary Science Reviews*, *83*, 58-67.

Dalibard, M., Popescu, S. M., Maley, J., Baudin, F., Melinte-Dobrinescu, M. C., Pittet, B., ... & Suc, J. P. (2014). High-resolution vegetation history of West Africa during the last 145 ka. *Geobios*, *47*(4), 183-198.

Davis, B. A., & Brewer, S. (2009). Orbital forcing and role of the latitudinal insolation/temperature gradient. *Climate dynamics*, *32*(2-3), 143-165.

De Lange, G. J., Thomson, J., Reitz, A., Slomp, C. P., Principato, M. S., Erba, E., & Corselli, C. (2008). Synchronous basin-wide formation and redox-controlled preservation of a Mediterranean sapropel. *Nature Geoscience*, *1*(9), 606.

Dekens, P. S., Lea, D. W., Pak, D. K., & Spero, H. J. (2002). Core top calibration of Mg/Ca in tropical foraminifera: Refining paleotemperature estimation. *Geochemistry, Geophysics, Geosystems*, *3*(4), 1-29.

Elderfield, H., Greaves, M., Barker, S., Hall, I. R., Tripati, A., Ferretti, P., ... & Daunt, C. (2010). A record of bottom water temperature and seawater δ 18 O for the Southern Ocean over the past 440kyr based on Mg/Ca of benthic foraminiferal Uvigerina spp. *Quaternary Science Reviews*, *29*(1), 160-169.

Emeis, K. C., Schulz, H., Struck, U., Rossignol-Strick, M., Erlenkeuser, H., Howell, M. W., ... & Sakamoto, T. (2003). Eastern Mediterranean surface water temperatures and δ18O composition during deposition of sapropels in the late Quaternary. *Paleoceanography and Paleoclimatology*, *18*(1).

Evans, D., & Müller, W. (2012). Deep time foraminifera Mg/Ca paleothermometry: Nonlinear correction for secular change in seawater Mg/Ca. *Paleoceanography and Paleoclimatology*, *27*(4).

Gasse, F. (2000). Hydrological changes in the African tropics since the Last Glacial Maximum. *Quaternary Science Reviews*, *19*(1-5), 189-211.

Geerken, E., Nooijer, L. J. D., Dijk, I. V., & Reichart, G. J. (2018). Impact of salinity on element incorporation in two benthic foraminiferal species with contrasting magnesium contents. *Biogeosciences*, *15*(7), 2205-2218.

Grant, K. M., Rohling, E. J., Bar-Matthews, M., Ayalon, A., Medina-Elizalde, M., Ramsey, C. B., ... & Roberts, A. P. (2012). Rapid coupling between ice volume and polar temperature over the past 150,000 years. *Nature*, *491*(7426), 744.

Grant, K. M., Grimm, R., Mikolajewicz, U., Marino, G., Ziegler, M., & Rohling, E. J. (2016). The timing of Mediterranean sapropel deposition relative to insolation, sea-level and African monsoon changes. *Quaternary Science Reviews*, *140*, 125-141.

Grazzini, C. V., Saliege, J. F., Urrutiaguer, M. J., & Iannace, A. (1990). 23. OXYGEN AND CARBON ISOTOPE STRATIGRAPHY OF ODP HOLE 653A AND SITE 654: THE PLIOCENE-PLEISTOCENE GLACIAL HISTORY RECORDED IN THE TYRRHENIAN BASIN (WEST MEDITERRANEAN).

Grimm, R., Maier-Reimer, E., Mikolajewicz, U., Schmiedl, G., Müller-Navarra, K., Adloff, F., ... & Emeis, K. C. (2015). Late glacial initiation of Holocene eastern Mediterranean sapropel formation. *Nature communications*, *6*, 7099.

Gonzalez-Mora, B., Sierro, F. J., & Flores, J. A. (2008). Controls of shell calcification in planktonic foraminifers. *Quaternary Science Reviews*, *27*(9-10), 956-961.

Hecht, A., & Gertman, I. (2001). Physical features of the eastern Mediterranean resulting from the integration of POEM data with Russian Mediterranean cruises. *Deep Sea Research Part I: Oceanographic Research Papers*, *48*(8), 1847-1876.

Hennekam, R., Jilbert, T., Schnetger, B., & Lange, G. J. (2014). Solar forcing of Nile discharge and sapropel S1 formation in the early to middle Holocene eastern Mediterranean. *Paleoceanography*, *29*(5), 343-356.

Hennekam, R., Donders, T. H., Zwiep, K., & de Lange, G. J. (2015). Integral view of Holocene precipitation and vegetation changes in the Nile catchment area as inferred from its delta sediments. *Quaternary Science Reviews*, *130*, 189-199.

Hönisch, B., Allen, K. A., Russell, A. D., Eggins, S. M., Bijma, J., Spero, H. J., ... & Yu, J. (2011). Planktic foraminifers as recorders of seawater Ba/Ca. *Marine Micropaleontology*, *79*(1-2), 52-57.

Hoogakker, B. A., Klinkhammer, G. P., Elderfield, H., Rohling, E. J., & Hayward, C. (2009). Mg/Ca paleothermometry in high salinity environments. *Earth and Planetary Science Letters*, *284*(3-4), 583-589.

Kageyama, M., Merkel, U., Otto-Bliesner, B., Prange, M., Abe-Ouchi, A., Lohmann, G., ... & Zhang, X. (2013). Climatic impacts of fresh water hosing under Last Glacial Maximum conditions: a multi-model study. *Climate of the Past*, *9*(2), 935-953.

Kısakürek, B., Eisenhauer, A., Böhm, F., Garbe-Schönberg, D., & Erez, J. (2008). Controls on shell Mg/Ca and Sr/Ca in cultured planktonic foraminiferan, Globigerinoides ruber (white). *Earth and Planetary Science Letters*, *273*(3-4), 260-269.

Klein, R. G. (2000). Archeology and the evolution of human behavior. *Evolutionary Anthropology: Issues, News, and Reviews*, *9*(1), 17-36.

Kontakiotis, G., Mortyn, P. G., Antonarakou, A., Martínez-Botí, M. A., & Triantaphyllou, M. V. (2011). Field-based validation of a diagenetic effect on G. ruber Mg/Ca paleothermometry: Core top results from the Aegean Sea (eastern Mediterranean). *Geochemistry, Geophysics, Geosystems*, *12*(9).

Kontakiotis, G., Antonarakou, A., Mortyn, P. G., Drinia, H., Anastasakis, G., Zarkogiannis, S., & Möbius, J. (2017). Morphological recognition of Globigerinoides ruber morphotypes and their susceptibility to diagenetic alteration in the eastern Mediterranean Sea. *Journal of Marine Systems*, *174*, 12-24.

Laskar, J. (1990). The chaotic motion of the solar system: A numerical estimate of the size of the chaotic zones. *Icarus*, *88*(2), 266-291.

Lea, D. W., & Spero, H. J. (1994). Assessing the reliability of paleochemical tracers: Barium uptake in the shells of planktonic foraminifera. *Paleoceanography*, *9*(3), 445-452.

Lourens, L. J. (2004). Revised tuning of Ocean Drilling Program Site 964 and KC01B (Mediterranean) and implications for the $\delta^{18}O$, tephra, calcareous nannofossil, and geomagnetic reversal chronologies of the past 1.1 Myr. *Paleoceanography*, *19*(3).

Marino, G., Rohling, E. J., Rijpstra, W. I. C., Sangiorgi, F., Schouten, S., & Damsté, J. S. S. (2007). Aegean Sea as driver of hydrographic and ecological changes in the eastern Mediterranean. *Geology*, *35*(8), 675-678.

Mellars, P. (2006). Archeology and the dispersal of modern humans in Europe: Deconstructing the "Aurignacian". *Evolutionary Anthropology: Issues, News, and Reviews: Issues, News, and Reviews*, *15*(5), 167-182.

Mezger, E. M., Nooijer, L. J., Boer, W., Brummer, G. J. A., & Reichart, G. J. (2016). Salinity controls on Na incorporation in Red Sea planktonic foraminifera. *Paleoceanography*, *31*(12), 1562-1582.

Mezger, E. M., de Nooijer, L. J., Siccha, M., Brummer, G. J. A., Kucera, M., & Reichart, G. J. (2018). Taphonomic and ontogenetic effects on Na/Ca and Mg/Ca in spinose planktonic foraminifera from the Red Sea. *Geochemistry, Geophysics, Geosystems*.

Nicholson, S. E. (2009). A revised picture of the structure of the "monsoon" and land ITCZ over West Africa. *Climate Dynamics*, *32*(7-8), 1155-1171.

Martrat, B., Grimalt, J. O., Shackleton, N. J., de Abreu, L., Hutterli, M. A., & Stocker, T. F. (2007). Four climate cycles of recurring deep and surface water destabilizations on the Iberian margin. *Science*, *317*(5837), 502-507.

Osborne, A. H., Vance, D., Rohling, E. J., Barton, N., Rogerson, M., & Fello, N. (2008). A humid corridor across the Sahara for the migration of early modern humans out of Africa 120,000 years ago. *Proceedings of the National Academy of Sciences*, *105*(43), 16444-16447.

Pena, L. D., Calvo, E., Cacho, I., Eggins, S., & Pelejero, C. (2005). Identification and removal of Mn-Mg-rich contaminant phases on foraminiferal tests: Implications for Mg/Ca past temperature reconstructions. *Geochemistry, Geophysics, Geosystems*, *6*(9).

Petraglia, M. D., & Rose, J. I. (2009). *The evolution of human populations in Arabia*. Springer, Dordrecht, Netherlands.

Pinardi, N., & Masetti, E. (2000). Variability of the large scale general circulation of the Mediterranean Sea from observations and modelling: a review. *Palaeogeography, Palaeoclimatology, Palaeoecology*, *158*(3-4), 153-173.

Pujol, C., & Grazzini, C. V. (1995). Distribution patterns of live planktic foraminifers as related to regional hydrography and productive systems of the Mediterranean Sea. Marine Micropaleontology, 25, 187– 217.

Rodrigues, D., Abell, P. I., & Kröpelin, S. (2000). Seasonality in the early Holocene climate of Northwest Sudan: interpretation of Etheria elliptica shell isotopic data. *Global and Planetary Change*, *26*(1-3), 181-187.

Rogerson, M., Rohling, E. J., Bigg, G. R., & Ramirez, J. (2012). Paleoceanography of the Atlantic-Mediterranean exchange: Overview and first quantitative assessment of climatic forcing. *Reviews of Geophysics*, *50*(2).

Reichart, G. J., Jorissen, F., Anschutz, P., & Mason, P. R. (2003). Single foraminiferal test chemistry records the marine environment. *Geology*, *31*(4), 355-358.

Rohling, E. J. (1994). Review and new aspects concerning the formation of eastern Mediterranean sapropels. *Marine Geology*, *122*(1-2), 1-28.

Rohling, E. J., & Bigg, G. R. (1998). Paleosalinity and δ18O: a critical assessment. *Journal of Geophysical Research: Oceans*, *103*(C1), 1307-1318.

Rohling, E. J., Cane, T. R., Cooke, S., Sprovieri, M., Bouloubassi, I., Emeis, K. C., ... & Kemp, A. E. S. (2002). African monsoon variability during the previous interglacial maximum. *Earth and Planetary Science Letters*, *202*(1), 61-75.

Rohling, E. J., Sprovieri, M., Cane, T., Casford, J. S. L., Cooke, S., Bouloubassi, I., ... & Jorissen, F. J. (2004). Reconstructing past planktic foraminiferal habitats using stable isotope data: a case history for Mediterranean sapropel S5. *Marine Micropaleontology*, *50*(1-2), 89-123.

Rohling, E. J., Grant, K. M., Roberts, A. P., & Larrasoana, J. C. (2013). Paleoclimate variability in the Mediterranean and Red Sea regions during the last 500,000 years: implications for hominin migrations. *Current Anthropology*, *54*(S8), S183-S201.

Rohling, E. J., Foster, G. L., Grant, K. M., Marino, G., Roberts, A. P., Tamisiea, M. E., & Williams, F. (2014). Sea-level and deep-sea-temperature variability over the past 5.3 million years. *Nature*, *508*(7497), 477.

Rohling, E. J., Marino, G., & Grant, K. M. (2015). Mediterranean climate and oceanography, and the periodic development of anoxic events (sapropels). *Earth-Science Reviews*, *143*, 62-97.

Rodrigues, D., Abell, P. I., & Kröpelin, S. (2000). Seasonality in the early Holocene climate of Northwest Sudan: interpretation of Etheria elliptica shell isotopic data. *Global and Planetary Change*, *26*(1-3), 181-187.

Rossignol-Strick, M., Nesteroff, W., Olive, P., & Vergnaud-Grazzini, C. (1982). After the deluge: Mediterranean stagnation and sapropel formation. *Nature*, *295*(5845), 105.

Rossignol-Strick, M. (1985). Mediterranean Quaternary sapropels, an immediate response of the African monsoon to variation of insolation. *Palaeogeography, palaeoclimatology, palaeoecology*, *49*(3-4), 237-263.

Rozanski, K. (1985). Deuterium and oxygen-18 in European groundwaters—links to atmospheric circulation in the past. *Chemical Geology: Isotope Geoscience section*, *52*(3-4), 349-363.

Schmuker, B., & Schiebel, R. (2002). Planktic foraminifers and hydrography of the eastern and northern Caribbean Sea. *Marine Micropaleontology*, *46*(3-4), 387-403.

Simon, M. H., Ziegler, M., Bosmans, J., Barker, S., Reason, C. J., & Hall, I. R. (2015). Eastern South African hydroclimate over the past 270,000 years. *Scientific reports*, *5*, 18153.

Singarayer, J. S., & Burrough, S. L. (2015). Interhemispheric dynamics of the African rainbelt during the late Quaternary. *Quaternary Science Reviews*, *124*, 48-67.

Steinhardt, J., de Nooijer, L. L., Brummer, G. J., & Reichart, G. J. (2015). Profiling planktonic foraminiferal crust formation. *Geochemistry, Geophysics, Geosystems*, *16*(7), 2409-2430.

Stringer, C. (2000). Palaeoanthropology: coasting out of Africa. *Nature*, *405*(6782), 24.

Thomson, J., Mercone, D., De Lange, G. J., & Van Santvoort, P. J. M. (1999). Review of recent advances in the interpretation of eastern Mediterranean sapropel S1 from geochemical evidence. *Marine Geology*, *153*(1-4), 77-89.

Tjallingii, R., Claussen, M., Stuut, J. B. W., Fohlmeister, J., Jahn, A., Bickert, T., ... & Röhl, U. (2008). Coherent high-and low-latitude control of the northwest African hydrological balance. *Nature Geoscience*, *1*(10), 670.

Tomczak, M., & Godfrey, J. S. (1994). *Regional oceanography: an introduction*. Elsevier.

Tribovillard, N., Algeo, T. J., Lyons, T., & Riboulleau, A. (2006). Trace metals as paleoredox and paleoproductivity proxies: an update. *Chemical geology*, *232*(1-2), 12-32.

van der Meer, M. T., Baas, M., Rijpstra, W. I. C., Marino, G., Rohling, E. J., Damsté, J. S. S., & Schouten, S. (2007). Hydrogen isotopic compositions of long-chain alkenones record freshwater flooding of the Eastern Mediterranean at the onset of sapropel deposition. *Earth and Planetary Science Letters*, *262*(3-4), 594-600.

Viehberg, F. A., Just, J., Dean, J. R., Wagner, B., Franz, S. O., Klasen, N., ... & Leng, M. J. (2018). Environmental change during MIS4 and MIS 3 opened corridors in the Horn of Africa for Homo sapiens expansion. *Quaternary Science Reviews*.

Vergnaud-Grazzini, C., Ryan, W. B., & Cita, M. B. (1977). Stable isotopic fractionation, climate change and episodic stagnation in the eastern Mediterranean during the late Quaternary. *Marine Micropaleontology*, *2*, 353-370.

Wang, Y., Cheng, H., Edwards, R. L., Kong, X., Shao, X., Chen, S., ... & An, Z. (2008). Millennial-and orbital-scale changes in the East Asian monsoon over the past 224,000 years. *Nature*, *451*(7182), 1090.

Wit, J. C., De Nooijer, L. J., Wolthers, M., & Reichart, G. J. (2013). A novel salinity proxy based on Na incorporation into foraminiferal calcite. *Biogeosciences*, *10*(10), 6375-6387.

Weldeab, S., Emeis, K. C., Hemleben, C., Schmiedl, G., & Schulz, H. (2003). Spatial productivity variations during formation of sapropels S5 and S6 in the Mediterranean Sea: evidence from Ba contents. *Palaeogeography, Palaeoclimatology, Palaeoecology*, *191*(2), 169-190.

Weldeab, S., Schneider, R. R., & Kölling, M. (2006). Comparison of foraminiferal cleaning procedures for Mg/Ca paleothermometry on core material deposited under varying terrigenous-input and bottom water conditions. *Geochemistry, Geophysics, Geosystems*, *7*(4).

Weldeab, S., Lea, D. W., Schneider, R. R., & Andersen, N. (2007). 155,000 years of West African monsoon and ocean thermal evolution. *science*, *316*(5829), 1303-1307.

Weldeab, S., Menke, V., & Schmiedl, G. (2014). The pace of East African monsoon evolution during the Holocene. *Geophysical Research Letters*, *41*(5), 1724-1732.

Williams, M. A., Adamson, D., Cock, B., & McEvedy, R. (2000). Late quaternary environments in the White Nile region, Sudan. *Global and Planetary Change*, *26*(1-3), 305-316.

Woodward, J. (Ed.). (2009). *The physical geography of the Mediterranean* (Vol. 8). Oxford University Press on Demand.

Wüst, G. (1961). On the vertical circulation of the Mediterranean Sea. *Journal of Geophysical Research*, *66*(10), 3261-3271.

Yoshimura, T., Tamenori, Y., Suzuki, A., Kawahata, H., Iwasaki, N., Hasegawa, H., ... & Ohkouchi, N. (2017). Altervalent substitution of sodium for calcium in biogenic calcite and aragonite. *Geochimica et Cosmochimica Acta*, *202*, 21-38.

Ziegler, M., Tuenter, E., & Lourens, L. J. (2010). The precession phase of the boreal summer monsoon as viewed from the eastern Mediterranean (ODP Site 968). *Quaternary Science Reviews*, *29*(11), 1481-1490.

Zwiep, K. L., Hennekam, R., Donders, T. H., van Helmond, N. A., de Lange, G. J., & Sangiorgi, F. (2018). Marine productivity, water column processes and seafloor anoxia in relation to Nile discharge during sapropels S1 and S3. *Quaternary Science Reviews*, *200*, 178-190.
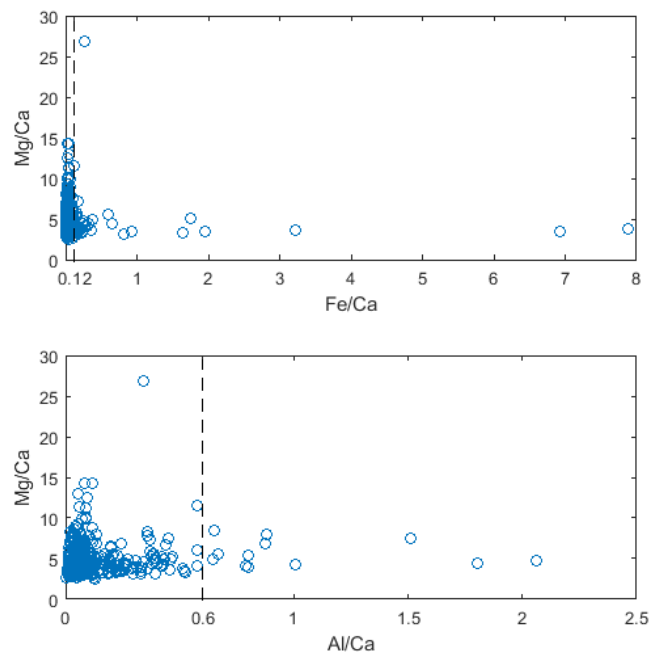
Appendix

Figure S1 | Mg/Ca versus Fe/Ca and Al/Ca. High Fe and Al ratios are considered indicators for contamination by clay particles. The maximum acceptable Fe/Ca and Al/Ca ratios are 0.12 and 0.6 mmol/mol. Samples with higher ratios are considered contaminated and therefore rejected for further analysis.
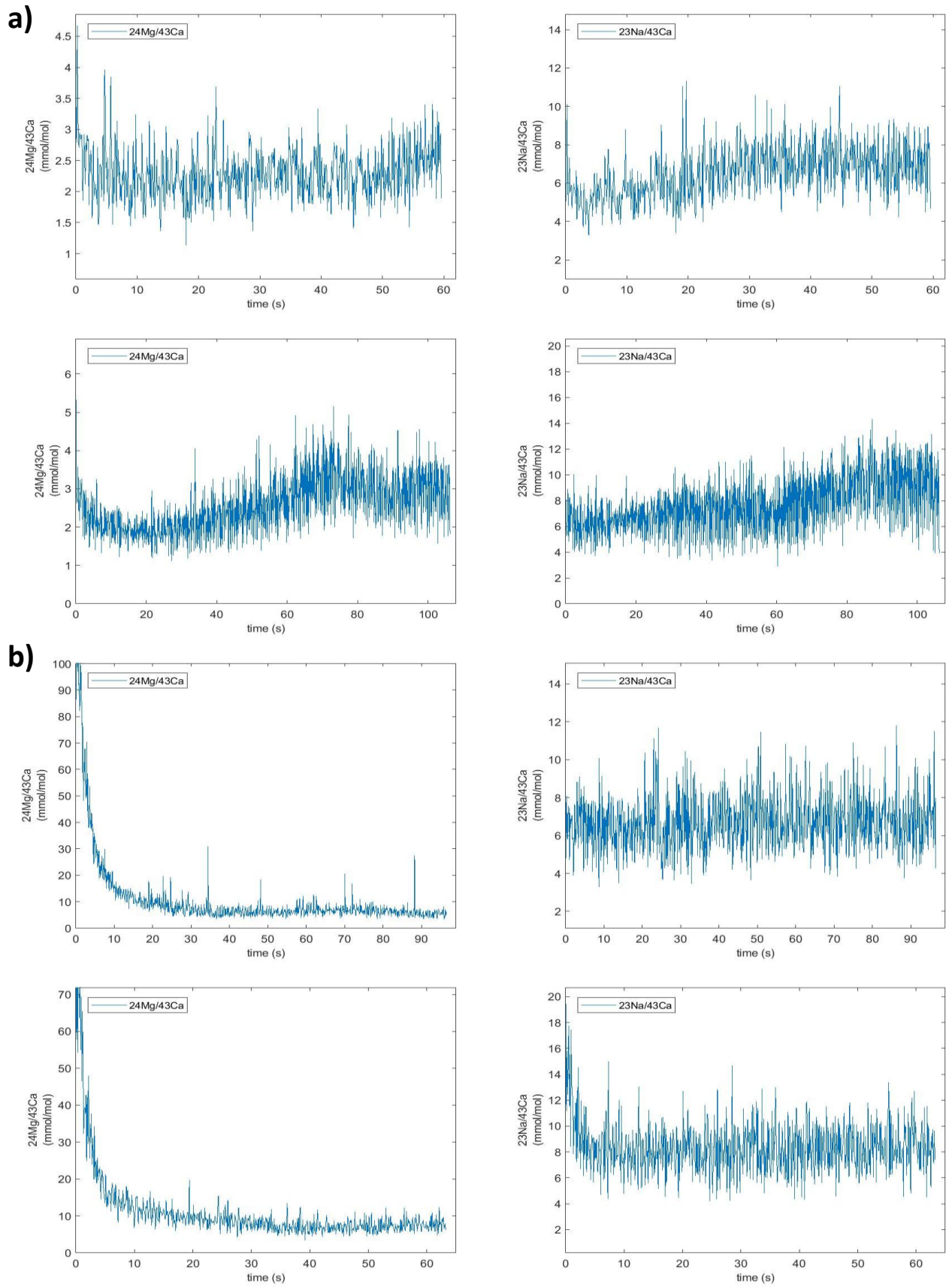
Figure S2 | Laser ablation profiles of *G. ruber* of sapropels (a) and non-sapropels (b). Note the high Na/Ca values and low Mg/Ca values in samples from sapropels and low Na/Ca and high Mg/Ca values in samples from non-sapropels.